

Review

Advanced Virgo: Status of the Detector, Latest Results and Future Prospects

Diego Bersanetti ^{1,*}, Barbara Patricelli ^{2,3}, Ornella Juliana Piccinni ⁴, Francesco Piergiovanni ^{5,6},
Francesco Salemi ^{7,8} and Valeria Sequino ^{9,10}

- ¹ INFN, Sezione di Genova, I-16146 Genova, Italy
² European Gravitational Observatory (EGO), Cascina, I-56021 Pisa, Italy; barbara.patricelli@pi.infn.it
³ INFN, Sezione di Pisa, I-56127 Pisa, Italy
⁴ INFN, Sezione di Roma, I-00185 Roma, Italy; ornella.juliana.piccinni@roma1.infn.it
⁵ Dipartimento di Scienze Pure e Applicate, Università di Urbino, I-61029 Urbino, Italy; francesco.piergiovanni@uniurb.it
⁶ INFN, Sezione di Firenze, I-50019 Sesto Fiorentino, Italy
⁷ Dipartimento di Fisica, Università di Trento, Povo, I-38123 Trento, Italy; francesco.salemi@unitn.it
⁸ INFN, TIFPA, Povo, I-38123 Trento, Italy
⁹ Dipartimento di Fisica “E. Pancini”, Università di Napoli “Federico II”, Complesso Universitario di Monte S. Angelo, I-80126 Napoli, Italy; valeria.sequino@na.infn.it
¹⁰ INFN, Sezione di Napoli, Complesso Universitario di Monte S. Angelo, I-80126 Napoli, Italy
* Correspondence: diego.bersanetti@ge.infn.it

Abstract: The Virgo detector, based at the EGO (European Gravitational Observatory) and located in Cascina (Pisa), played a significant role in the development of the gravitational-wave astronomy. From its first scientific run in 2007, the Virgo detector has constantly been upgraded over the years; since 2017, with the Advanced Virgo project, the detector reached a high sensitivity that allowed the detection of several classes of sources and to investigate new physics. This work reports the main hardware upgrades of the detector and the main astrophysical results from the latest five years; future prospects for the Virgo detector are also presented.

Keywords: gravitational waves; advanced virgo; interferometer; suspensions; optics; squeezing; multi-messenger astronomy; neutron stars; black holes; data analysis methods



Citation: Bersanetti, D.; Patricelli, B.; Piccinni, O.J.; Piergiovanni, F.; Salemi F.; Sequino V. Advanced Virgo: Status of the Detector, Latest Results and Future Prospects. *Universe* **2021**, *7*, 322. <https://doi.org/10.3390/universe7090322>

Academic Editor: James Overduin

Received: 13 July 2021

Accepted: 9 August 2021

Published: 30 August 2021

Publisher's Note: MDPI stays neutral with regard to jurisdictional claims in published maps and institutional affiliations.



Copyright: © 2021 by the authors. Licensee MDPI, Basel, Switzerland. This article is an open access article distributed under the terms and conditions of the Creative Commons Attribution (CC BY) license (<https://creativecommons.org/licenses/by/4.0/>).

1. Introduction

Gravitational waves (GWs) are transverse perturbations of the space-time metric produced by non-spherically symmetric accelerating masses. As predicted by general relativity, a passing gravitational wave will create alternating compression and expansion at orthogonal angles, i.e., producing a measurable strain in the space-time fabric. Two polarizations are permitted in standard general relativity: the plus-polarization, $+$, and the cross-polarization, \times , which is the plus-polarization rotated by 45 degrees.

Gravitational waves encode several physical properties of their astrophysical sources, such as, for binaries, the component masses, spins, sky location, and distances. Unlike electromagnetic radiation, gravitational waves can pass through any intervening matter without being scattered significantly [1]. Moreover, some astrophysical phenomena such as a merger of binary neutron stars, a neutron star—black hole merger, or a core-collapse supernova are expected to emit gravitational and electromagnetic waves, and neutrinos: GW detections potentially enable multimessenger studies of these objects.

Since 2015, more than 50 gravitational-wave events have been directly detected by the Laser Interferometer Gravitational-Wave Observatory (LIGO) [2] and the Virgo [3] detectors, all emitted by binary compact objects and reported in the 1st and the 2nd Gravitational-Wave Transient Catalogs, respectively GWTC-1 [4] and GWTC-2 [5].

In this work, we review the status of the Virgo detector and the main achievements reached in the field of GW astronomy in the last few years. The paper is organized as

follows: Section 2 gives a broad outline of the main astrophysical sources of gravitational waves and Section 3 describes the Italian gravitational-wave infrastructures; the main body of the paper is composed of Section 4, reporting a detailed description of the Advanced Virgo interferometer, Section 5, focusing on its performance during the latest observing run and Section 6, reviewing data analysis techniques and main scientific results; finally, we discuss future prospects for the Advanced Virgo project in Section 7 and conclude with Section 8.

2. Astrophysical Sources

The main astrophysical sources of GWs in the frequency range at which ground-based interferometers are sensitive (10 Hz–10 kHz) are: coalescing binary systems of compact objects (CBCs) composed by neutron stars (NSs) and/or stellar-mass black holes (BHs), core-collapsing massive stars and isolated NSs. Along with the more standard searches for GW from NSs or BHs, interferometric data can be used to look for more exotic signals such as those associated with Dark Matter (DM) candidates or with sources from the early universe.

CBC systems emit GWs detectable by current GW detectors in the last moments of their life: during the last orbits of the inspiral phase, during the merger phase and potentially during the post-merger phase. These events are very energetic: for instance, for GW150914 the energy radiated in GWs has been estimated to be $\sim 3 M_{\odot}$ [6]; the GW radiation from these systems is accurately modeled by post-Newtonian approximation for the inspiral phase, numerical relativity simulations for the merger phase and general-relativistic perturbation methods for the ringdown (if the remnant is a BH), therefore the GW signals are typically searched with the “matched filter modeled searches” (see Section 6). NS-NS and possibly NS-BH merging systems are also expected to emit electromagnetic (EM) radiation (see [7] for a review). They are thought to be the progenitors of short Gamma Ray Bursts (GRBs): intense and highly variable flashes of γ -rays whose duration is < 2 s (the prompt emission), sometimes followed by a long-lasting afterglow emission at lower energies (X-rays, optical, radio); these systems are also expected to isotropically eject a quantity of neutron-rich matter; the radioactive decay of heavy nuclei that are synthesized in this ejecta through r-processes produces a thermal optical/NIR emission: the “kilonova”. Finally, the interaction of the merger ejecta with the interstellar medium can produce a radio blast wave emission. The association between NS-NS mergers and short GRBs and kilonovae has been recently confirmed with the multi-messenger observation of GW170817 (see Section 6.3.3), while no EM emission has been observed so far in association with NS-BH mergers. Stellar-mass BH-BH mergers are generally not expected to have EM counterparts due to the absence of baryonic matter left outside the merger remnant; however, in recent years several scenarios predicting the presence of matter around these systems have been proposed (see, e.g., [8,9]) and recently a candidate optical counterpart to the BH-BH merger GW190521 has been reported [10].

Core-collapsing massive stars (stars with masses larger than $8 M_{\odot}$ at their final evolutionary stage) are expected to emit GWs if there is some asymmetry in the stellar envelope ejection phase (see [11–13] for an overview). Large uncertainties are affecting our knowledge on the collapsing phase of these objects, therefore the amount of GW energy released is highly uncertain as well: multidimensional core-collapse simulations predict the GW energy to be in the range between $10^{-11} M_{\odot} c^2$ and $10^{-7} M_{\odot} c^2$, but higher values are allowed when more extreme GW emission scenarios, such as long-lived bar-mode instabilities, are considered (see [14] and references therein). As a consequence, there is large uncertainty also in the maximum distance at which these sources can be detected: if the realistic models are considered, they could be detected by ground-based GW detectors within our Galaxy, while for the extreme scenarios they can be detected up to hundreds of Mpc [14]. Due to the uncertainty in the modeling of the GW signal, GWs from core-collapsing massive stars are searched with the so-called “unmodeled searches” (see Section 6). The core-collapse of a massive star is accompanied by the emission of EM radiation. Specifically, a supernova

(SN) emission at optical and radio frequencies is generally observed starting from days to weeks after the collapse and it lasts from weeks (optical) to years (radio). Such optical and radio emission can be preceded by a bright UV/X-ray flash of radiation produced when the shock wave generated by the collapsing core reaches the surface of the star: this is the so-called “shock break-out” (SBO) emission (see, e.g., [15,16]). Furthermore, there is observational evidence of the association between core-collapse of massive stars and long GRBs that are characterized by a longer duration (>2 s) of the prompt emission and a softer spectrum with respect to short GRBs (see, e.g., [17,18]). Finally, during core-collapse supernovae also neutrinos are emitted, as confirmed by the detection of MeV neutrinos from SN 1987A [19–21]. In addition, GRBs and SNe are expected to produce relativistic outflows in which protons and nuclei can be accelerated; such particles can produce high energy neutrinos by interacting with the surrounding medium and radiation (see, e.g., [22]).

Isolated NSs can emit GWs through different mechanisms (see [23] for a review). For instance, rotating NSs with very intense magnetic fields, of the order of 10^{15} G, can undergo starquakes (see, e.g., [24]): when this happens, asymmetric strains can temporarily modify the geometry of the star and GWs are expected to be emitted (see, e.g., [25]). The expected amount of GW energy emitted is highly uncertain (it might be in the range $10^{-16} M_{\odot} c^2$ – $10^{-6} M_{\odot} c^2$) and the GW waveform is uncertain as well, therefore the corresponding GW signals are searched with the unmodeled searches (see Section 6). EM phenomena possibly associated with these starquakes include soft gamma repeaters and anomalous X-ray pulsars, which are sporadic emissions of short bursts of gamma-rays and X-rays (see [26] for a review). GW emission associated to starquakes can also be accompanied by a radio/X-ray pulsar glitch: a sudden increase in the rotational frequency of the pulsar, followed by exponential decays, which bring back the pulsar to the initial value (see e.g., [27]).

Fast-spinning NSs are also expected to emit GWs continuously if they are asymmetric with respect to their rotation axis [28]. This happens both for isolated NSs or NSs in accreting systems like X-ray binaries. Potential targets are galactic sources. The energy released, as the star spins, is almost monochromatic and with a frequency proportional to the star’s spin frequency. Although the GW emission mechanism is widely understood, the actual factors which cause the asymmetry in the star are still under debate. Some scenarios include the possibility that the asymmetry is due to the presence of residual crustal deformations (e.g., after a fast cooling of the NS crust causing its breaking), the presence of a strong inner magnetic field not aligned with the star’s rotation axis, or the presence of magnetic or thermal “mountains” (see [23] for a review). The maximum ellipticity (i.e., deformability) the star can sustain depends on both the NS equation of state (EOS) and the breaking strain of the crust [29].

Different methods are used to search for these signals (see Section 6), also known as continuous waves (CW), according to the information available about the source. If the sky position of the source and its rotational parameters are known from EM observations, the so-called “targeted” or “narrow-band” searches are done using matched filtering (see, e.g., [30–33]). When only the sky position of an interesting source is known (or known with a small uncertainty), “directed” searches are performed, e.g., looking for supernova remnants [34–36] or sources in interesting sky regions like the Galactic Center or globular clusters [37], where a huge number of CW emitters are expected to be present. In this case, both modeled or unmodeled searches can be applied. Finally, when no parameter about the source is known, blind “all-sky” searches are performed (see, e.g., [38,39]). In this case, unmodeled or template-grid searches are used. For a review of CW signals and associated searches, see [40,41]. No transient or continuous GW emission from isolated NSs has been observed so far. The future detection of this type of signal would shed light on the internal structure of NS, hence on the EOS, given the relation of the GW amplitude to the star’s moment of inertia and the star’s ellipticity. CWs are then unique probes of the fundamental interactions happening inside NSs, which represent themselves as ideal laboratories to test fundamental physics and high-energy astrophysics in the strong-gravity regime [42].

The superposition of GW signals from various unresolved astrophysical and cosmological sources can generate a stochastic GW background (SGWB). The main sources that can contribute to the SGWB are: Core-Collapse SuperNovae (CCSNe) [43–45], NSs, CBCs, cosmic strings [46–48] and GWs produced during inflation [49–51]; among them, the most promising contribution for ground-based GW detectors come from CBCs that might be detectable by Advanced LIGO and Advanced Virgo at design sensitivity (see, e.g., [52]). The detection of the SGWB can provide unique information about astrophysical source populations (for instance, the merger rate of compact binary systems and the star formation history) and the physical processes in the very early Universe. No evidence for SGWB has been found so far, and upper limits on the GW background energy density have been placed.

GW detectors can also be exploited in the search for evidence of DM [53] (see Section 6.3.6). In the last couple of years, a brand-new branch of investigations of DM candidates using interferometric detectors took place. Although the principal aim of experiments like Virgo is to directly detect the GW strain produced by compact objects like BH and NS, the same principle can be used to investigate the effects of DM particles. This can be achieved by looking for particles directly interacting with the detector and/or for GW signatures produced by DM particles in the proximity of astrophysical objects; for a review of all the DM candidates that can be investigated using GWs, see [54].

A good fraction of DM particles could be represented by ultra-light bosons, including dark photons or Quantum-Chromo-Dynamics axions [55–57]. Gravitational wave detectors can also search for primordial black holes, i.e., small black holes below 1.5 solar masses, resulting from density fluctuations in the very early Universe [58]. These primordial BHs are supposed to contribute to a fraction of the dark matter energy density [59].

3. A Brief Historical Background of Italian GW Research Infrastructures

The prospect of opening a new window to investigate the Universe and the wealth of astrophysical properties that can be measured through GWs (briefly highlighted in the previous section) clearly motivated the development of GW experiments but, given the smallness of the expected signals and the related technological challenges, the path from theory to detection has been long and non-trivial.

In the 1970s, a new attitude of the scientific community towards Einstein's theory of gravitation—as well as the attention drawn by Joseph Weber's claims [60]—led to the formation of various GW groups all over the world; among those, the Rome group, established by Edoardo Amaldi and Guido Pizzella in 1970, was the first experimental GW group in Italy [61].

Their main project was building a cryogenic resonant bar detector, as part of an international collaboration with the Stanford University and Louisiana State University groups. The idea behind this kind of detectors was that, on the occurrence of a catastrophic gravitational collapse of astrophysical origin, the incoming GW, while impinging on an aluminum bar cooled to liquid He temperatures, exerts a tidal force causing the object to resonate at its characteristic resonant frequency, i.e., depositing a tiny yet measurable quantity of energy.

The cryogenic and ultra-cryogenic bar detectors that were built in the following 25 years were the reference for GW experiments. In particular, the last to be built, which are Explorer [62,63] (hosted at CERN), Nautilus [64,65] (hosted at the INFN laboratories of Frascati) and Auriga [66,67] (hosted at the INFN laboratories of Legnaro), formed, together with the Allegro detector at Louisiana State University [68] and Niobe at the University of Western Australia [69], the first global network of GW detectors, within the framework of the International Gravitational Events Collaboration (IGEC) [70–72].

Though such detectors failed to achieve the sensitivity needed to detect GWs, they paved the way for the laser interferometers. Italian universities and INFN [73] played a crucial role in this early stage of the experimental GW field by fostering various technological developments and training a whole generation of physicists.

In the meanwhile, the idea of a laser interferometric detector measuring the relative motion of test mass mirrors had been gaining momentum: this new approach was tested on prototype test facilities, while accumulating evidence for the viability of larger km-scale interferometers, both in the USA and Europe.

During the 1980s, both the LIGO and Virgo design studies were reaching maturity, which then led to the official proposals towards the end of the decade; here we will focus on the European project, Virgo: the initial proposal for a “long baseline interferometric antenna for the search of gravitational waves” [74] dates back to 1987, when Adalberto Giazotto and Alain Brillet, respectively from the Italian INFN [73] (Pisa division) and the French CNRS [75], together with other scientists, compiled the proposal of a project for an interferometric detector for gravitational waves. This proposal integrated the experience of the IRAS (“Interferometro per la Riduzione Attiva del Sisma”—Interferometer for Seismic noise Active Reduction) [76] experiment, which proved that a strong reduction of the residual seismic motion could be effectively implemented using Superattenuators [77], which are passive, multi-stage inverted pendulum systems apt to reduce this disturbance up to frequencies in the range of 10 Hz. The integration of this kind of attenuation system proved that interferometers could reach appreciable sensitivity also at low frequency, and this possibility was one of the key points of the Virgo proposal.

The Virgo project, which takes its name from the Virgo Cluster—deemed a candidate region for gravitational waves sources—was effectively approved in 1993–1994 from the two funding agencies, and the construction effort started in 1996 [78].

The chosen site for the detector was Cascina, near Pisa (IT) (see Figure 1). Here, the INFN and the CNRS built the full infrastructure needed for the detector, including 6 km of ultra-high vacuum tubes, where the long arm cavities would be placed. Such infrastructure is Europe’s largest under vacuum facility [79].



Figure 1. Aerial view of the Virgo site in Cascina (Pisa, Italy). Credit: The Virgo Collaboration.

In 2000, the European Gravitational Observatory (EGO) consortium was founded by INFN and CNRS and tasked with the supervision, the construction and the operation of the detector, under the direction of the two funding agencies.

In June 2003, when the construction of the initial Virgo detector was finally completed, the commissioning of the detector finally started, which took the instrument to the first

full lock in 2005; then, a series of data taking runs took place, between 2007 and 2011, with increasingly better sensitivity, mostly in coincidence with the two LIGO detectors. In particular, the LIGO-Virgo Memorandum of Understanding [80] of 2007 was a very important step towards GW astronomy: it stipulated a scientific collaboration between the two entities, with the crucial aspect of a joint analysis of the data coming from the three detectors.

However, despite the long standing effort and the achievement of the design sensitivity for all detectors (for Virgo see [81]), no GW event was detected during these initial runs and both LIGO and Virgo collaborations pressed ahead with their plans for consistent hardware upgrades, in order to bring the detectors to the “Advanced”, or 2nd Generation, era [82].

As the Advanced LIGO project managed to start earlier, the two Advanced LIGO detectors could complete their construction and commissioning phase already in 2015, while Advanced Virgo was able to join them in 2017 during the second Observing Run (O2); therefore, only the two LIGO detectors were online at the time of the first detection of gravitational waves (event GW150914 [83]) during the first Observing Run (O1), but in the LIGO-Virgo collaborative framework the joint data analysis and publication marked an historic landmark for the whole collaboration.

When Virgo came back online in August 2017, for the last part of the O2 Observing Run, the three detectors were finally working together again, and this achievement was rewarded with the two paramount triple-detector detections: the coalescence of a BH-BH system (event GW170814 [84]) and the inspiral of a NS-NS system (event GW170817 [85]), which marked the start of the multi-messenger astronomy, as the GW detection triggered the successful search for EM counterparts of the same event. For the first time GW detectors, EM telescopes and satellites, neutrino detectors and others worked in collaboration in order to achieve a full description of such an event from every point of view.

After the end of the O2 Run, both LIGO and Virgo underwent a long period of upgrade, installation and commissioning. The following O3 Run started synchronously for all detectors on 1 April 2019; the run, which was divided in two segments (O3a and O3b) with a commissioning intermission between the two, lasted almost one calendar year, as it concluded about a month early due to the COVID-19 pandemic.

The era of gravitational wave detection officially started, as the increased sensitivities of the instruments guaranteed a much higher rate of events, which collectively stacked up to ~ 50 , and were publicly released in the two catalogs GWTC-1 [4] and GWTC-2 [5].

After the end of the O3 Run, the detectors underwent another period of installation, upgrade and then commissioning, currently undergoing, which will bring the detectors to their next phase, the “Advanced [Virgo/LIGO] Plus” era; in such phase, LIGO and Virgo will be joined by the KAGRA detector [86], which already implements some of the 3rd generation technologies, like cryogenic test masses.

During this long process, the Virgo Collaboration (which started as a French-Italian joint venture back at the end of the 1980s, as described above) has steadily grown over time, with several institutions from many European countries joining the Collaboration at different times and starting to contribute to the experiment. One of the more long-standing and important contributors, Nikhef [87] (NL), has recently joined the EGO consortium, sharing now important responsibilities with INFN and CNRS.

INFN itself has grown substantially its presence in the Collaboration, with several other divisions joining at different times the collaboration, in addition to the founding ones, taking responsibility for many important parts of the detector, as for example the Suspension system (developed from the original idea from Giazotto et al.), the Payloads (Section 4.2.1) and the Thermal Compensation System (Section 4.3.2), while important contributions are present also regarding Mirrors and Optics (Section 4.2.2), Controls (Section 4.3.1), the Squeezing system (Section 4.2.3) and other items of the detector.

Moreover, these contributions, which are heavily focused on the infrastructure and the hardware of the detector, several others have been carried out by many INFN physicists

from many divisions, contributing to the analysis of the Virgo data, from the development of techniques and pipelines to astrophysical investigations, statistical analysis and multi-messenger astronomy.

To these two macro-areas an important part of the rest of the paper will be devoted, to tackle and describe both the instrument and the data analysis regarding the Advanced Virgo project.

4. The Advanced Virgo Detector

As stated in Section 3, Advanced Virgo is a laser interferometer, and its working principle is the destructive interference pattern of a Michelson interferometer: a monochromatic laser field is injected inside the interferometer and split equally among the two arms; such arms reflect the fields back, and they are then recombined and then sent towards the detection port of the interferometer.

The magnitude and the complexity of the measurement pose great requirements to the setup of the detector which, therefore, deviates substantially from the standard Michelson interferometer, while the working principle remains the same. In this section, a full description of the detector will be presented, from the actual optical layout in operation in the detector (Section 4.1) to the many technological solutions which have been invented and exploited in order to maximize the performance and the stability of the detector (Section 4.2).

4.1. Optical Layout

As stated at the beginning of this section, the working principle of the Virgo experiment is the Michelson interferometer, tuned in the dark fringe configuration. Due to the very strong requirements on the detector's sensitivity, though, the actual optical configuration is much more complicated and it is focused on the maximization of the detector's performance: an extensive use of resonant optical cavities is made, for several reasons that will be explained shortly.

In Figure 2 the optical layout of Advanced Virgo is depicted; in the following we describe its main parts.

- The Injection system (left part of Figure 2): here the main laser beam is generated, from a 1064 nm Nd:YAG laser source; such laser is pre-stabilized in both amplitude and frequency before actually being injected inside the interferometer, but other fundamental components are necessary at this stage. The main laser beam is passed through an Electro-Optical Modulator (EOM) which generates several radio-frequency sidebands for the carrier light, which are necessary for the Global Control of the interferometer (6 MHz, 8 MHz and 56 MHz, cf. Section 4.3.1) or the control of the Injection system itself (22 MHz). Then, the laser beam (now carrier plus sidebands) is sent into a triangular resonant cavity, the Input Mode Cleaner (IMC), which serves the purpose of both cleaning the laser field from high order modes, in order to inject as much as possible in the interferometer only the TEM₀₀ fundamental mode, and providing an additional stage of frequency stabilization. An additional short, rigid cavity (Reference Cavity, RFC) is used to control the IMC cavity length, such to provide an additional laser frequency stabilization also at low frequency. Then, the laser beam is injected in the main interferometer.
- The main interferometer (central and right part of Figure 2): it is composed by the seven main optics which form this enhanced Michelson configuration; in the middle, the Beam Splitter (BS) mirror equally splits the incoming light and sends it in the two arms of the interferometer. Differently from the standard Michelson interferometer, in Virgo the arms (North and West) are not composed by a single reflecting mirror at the end of each arm, but rather by a resonant Fabry-Pérot 3 km long cavity made by two highly reflective mirrors, with the reflecting sides facing one another. The use of Fabry-Pérot cavities makes so that the light can be trapped inside the arm for many round trips, before being reflected back or transmitted: this causes the big

advantage that the effective arm length of the interferometer is amplified by a factor $\frac{2\mathcal{F}}{\pi} \approx 300$ (where $\mathcal{F} \approx 460$ is the Finesse of the arm cavities), therefore increasing the detector sensitivity. Since the interferometer working point is dark fringe, this means that most of the light, once reflected by the arms and recombined by the BS mirror, is sent back toward the Injection system; therefore, a semi-reflective mirror is added between the Injection system and the Fabry-Pérot Michelson, in order to create with the latter another resonant cavity: this Power Recycling (PR) mirror reflects this rejected light back into the main interferometer, effectively increasing the circulating power of the laser field in the detector. With the same principle, but for a different outcome, a similar Signal Recycling (SR) mirror is added between the output port of the Fabry-Pérot Michelson and the main part of the Detection system: another resonant cavity is therefore present, with the purpose of recirculating the signal used for the detection, allowing shaping the sensitivity curve of the interferometer (see Section 7.1). However, this mirror has not been used in Advanced Virgo yet and it has been replaced by a simple lens; its full implementation is foreseen for the O4 Observing Run.

- The Detection system (bottom part of Figure 2 and outputs of the main resonant cavities): this is a more distributed system, but its main part is at the output of the main interferometer and deals with the collection, cleaning and the enhancement of the output beam after the recombination from the BS mirror, which is the signal used for the detection of gravitational waves. Such signal is passed through two Output Mode Cleaner (OMC) cavities: two monolithic, bow-tie shaped cavities, which provide the cleaning of the signal from any sideband field, as these are not necessary in the Advanced Virgo detection scheme [88]; the OMCs also provide an additional step of removal of high order modes. The beam is then collected by the main photodiode (B1). Several other photodiodes (PD) and quadrant photodiodes (QPD) are installed in the main output ports of the interferometer (B2 at the input port, B7 at North End, B8 at West End) or in the central area (B4 as a pick-off of the Power Recycling cavity, B1p as a pick-off of the output beam before the removal of the sidebands and B5 as a pick-off from the anti-reflective side of the BS mirror, sensitive mostly to the North Arm). All the PDs and QPDs (and the OMCs) are installed on under-vacuum, controlled Suspended Benches, in order to mitigate the effect of several sources of noise.

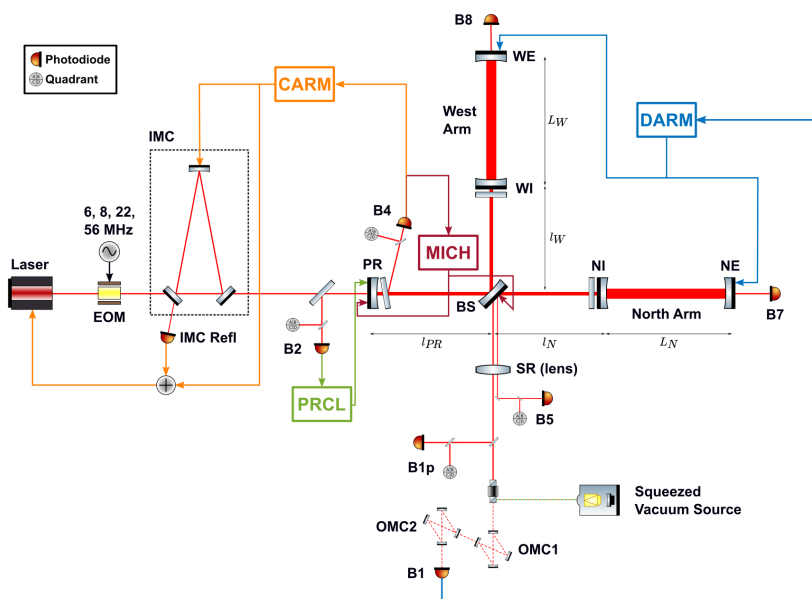


Figure 2. Optical layout of Advanced Virgo during O3. Each depicted Quadrant Photodiode (QPD) actually represents a set of two different physical sensors [89]. DARM, CARM, MICH and PRCL refer to the longitudinal degrees of freedom (cf. Section 4.3.1).

4.2. Technological Solutions for Advanced Virgo's Sensitivity

The design sensitivity of a gravitational waves ground-based detector is given by the quadratic sum of the contribution from all the noise sources affecting the detector output. In Figure 3 the amplitude spectra are shown for all the main fundamental noise sources of the Advanced Virgo detector [3].

With the upgrade from Virgo to Advanced Virgo an average gain of one order of magnitude for a large part of the frequency band (10 Hz–10 kHz) was obtained. To obtain this huge improvement an extraordinary effort was needed, which included large infrastructure investments, the re-design of many parts of the interferometer, and years of R&Ds to find new technological solutions or enhance the existing ones. A detailed description of all the Advanced Virgo subsystems can be found in the Technical Design Report [82]. In the following of this section, an analysis of the main noise sources which affect the different frequency regions of the Advanced Virgo sensitivity curve is presented. Moreover, a description of the main systems which allows the mitigation of these noises is given.

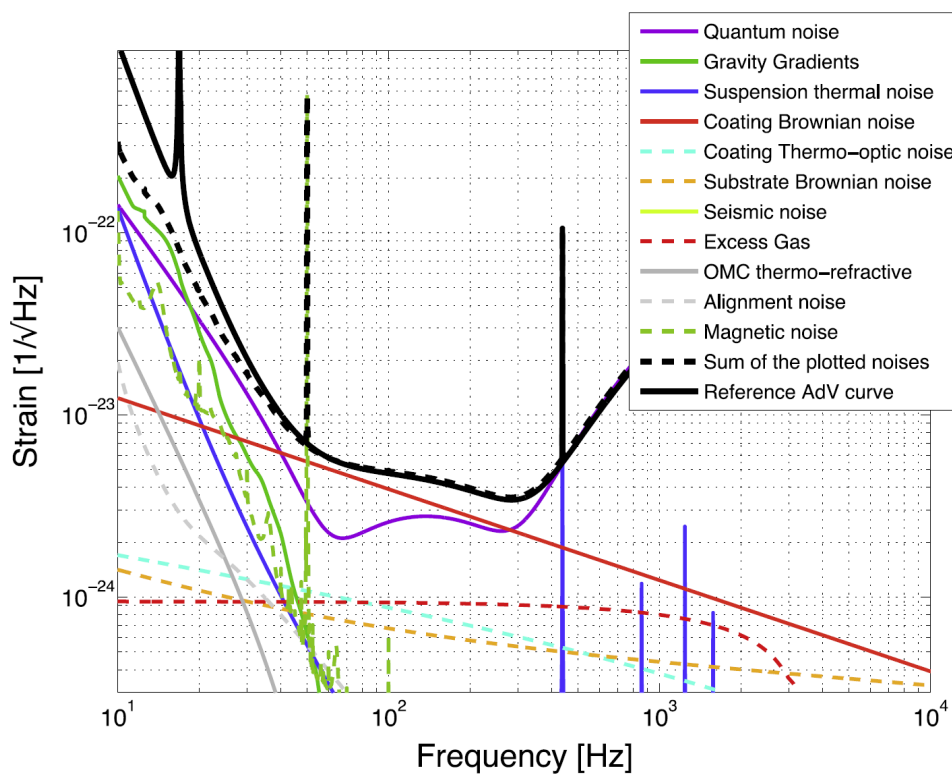


Figure 3. The noise (dashed black lines) computed as the sum of all the known noise contributions, is compared to a reference AdV sensitivity (solid black line). The contributions from all the single noise sources are also shown. Figure taken from [90]: © The Authors, published by EDP Sciences. This is an open access article distributed under the terms of the Creative Commons Attribution License 4.0 (<http://creativecommons.org/licenses/by/4.0/> (accessed on 10 August 2021)).

4.2.1. Low Frequency: Suspensions & Payloads

Gravity gradients, seismic movements of the ground, and molecular thermal agitation of the mirror suspensions are the main noise sources which determine the detector sensitivity limits in the low frequency region starting from 10 Hz to 40 Hz.

The Newtonian noise: the motion of test masses produced by terrestrial density fluctuations in the surroundings of the detector is called gravity gradient or Newtonian noise (NN). Sources of NN are natural and infrastructural seismic waves, atmospheric mass movements (among others), which can perturb in a not shieldable manner the local gravity field [91,92]. Accurate measurements from seismometer arrays and tiltmeters are needed

to model the seismic motion in order to perform an effective noise cancellation [93,94]. A recent work [95] shows that NN in Virgo is suppressed by about a factor of two at 15 Hz by clean rooms and recesses underneath the test masses, suggesting that the infrastructural design could have a strong impact in NN mitigation. In Advanced LIGO and Advanced Virgo the NN starts to be relevant only under 20 Hz just near the lower limit of the detector band, nevertheless NN suppression will be mandatory both for the next version of the current detectors and for the next detector generations which will extend the frequency range towards the 1 Hz region [96].

The seismic noise and the Superattenuator: to enable the detection of the tiny deformations in the detector arms induced by a gravitational wave, the test masses must be isolated from the continuous vibration of the ground. An attenuation of more than ten orders of magnitude above 10 Hz on all the degrees of freedom is needed [3]. A very complex suspension system has been designed and realized for the Virgo detector: the Superattenuator (SA). The SA is composed of a five-stage pendulum hanging the last stage of suspension (the payload) which includes the test mass [97]. The horizontal vibration attenuation from the top to the bottom of the pendula chain, decreases as $1/f^{2N}$ for frequencies above the SA resonant modes, N being the number of stages. Moreover, the top of the chain is suspended to a platform ring supported by three legs that are connected to the bottom ground by elastic joints. The aim of this inverted pendulum is to obtain a further reduction of the amount of seismic horizontal ground vibrations which reach the payload. The overall height of the system is about 8 m, in order to confine all the resonance modes below 2 Hz. In Figure 4 a scheme of the SA is shown.

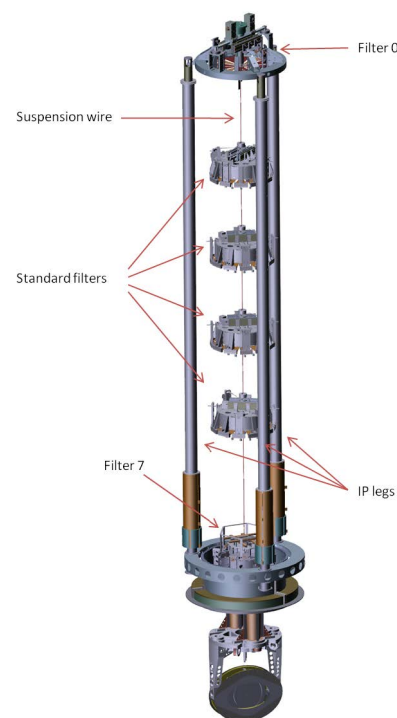


Figure 4. A scheme of the Virgo SA system. The filter chain starts with filter 0 at the top of the three legs of the inverted pendulum. Four standard intermediate filters and filter 7 complete the chain. The payload, composed of marionette, mirror and cage, is hung to filter 7. Credits: INFN Pisa.

Although in principle the detector signal can only be perturbed by horizontal movements, earth curvature and unavoidable tiny mechanical imperfections of the suspension system produce a coupling between vertical motion of the ground and fluctuation of the horizontal distance of the test masses. The estimated vertical to horizontal coupling factor is of the order of 10^{-3} . For this reason, the SA must provide also for a vertical isolation system. Each mass of the pendula chain is composed of a series of concentric flexible blades

supporting the wire of the stage below. To lower the vertical resonant mode frequencies below 2 Hz, the low stiffness blades are aided by a magnetic anti-spring system.

The payload, which is the last stage of the suspension, is hung to the lowest filter of the chain (filter 7). It is basically a double pendulum [98], in which the mirror is suspended to a penultimate steel body called marionette. The double pendulum is surrounded by a cage (suspended to filter 7), which is designed to serve as a reference mass. The cage is equipped with sensors and actuators for positioning control, and also contains the baffles for stray light control, and the elements of the thermal compensation system (cf. Section 4.3.2). A scheme of the payload is shown in Figure 5.

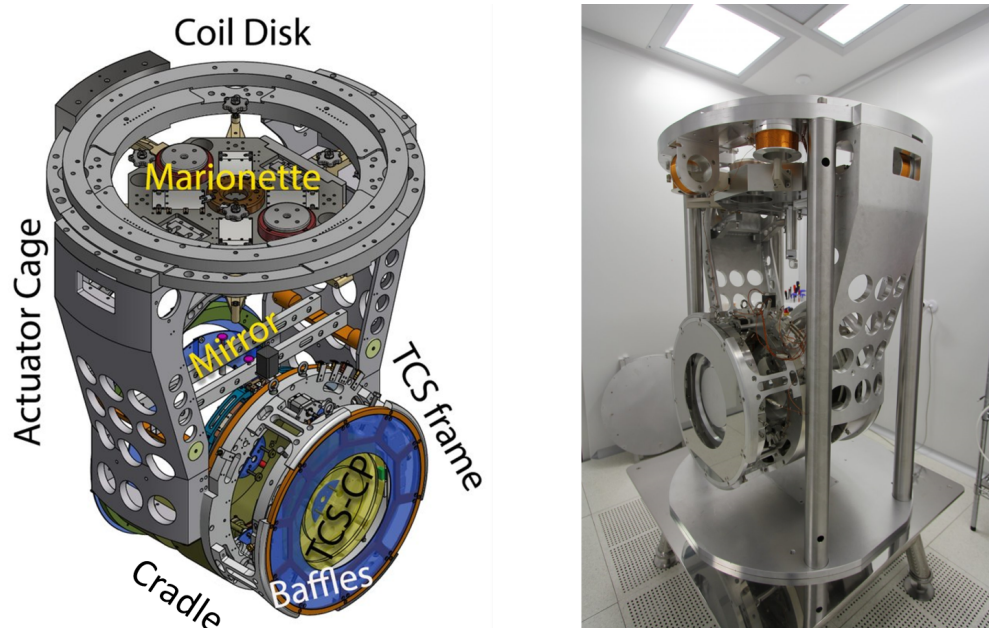


Figure 5. A scheme (on the left), and the assembly in clean room (on the right) of the Advanced Virgo payload [99]. Besides the suspension elements—mirror, marionette and actuator cage—the components belonging to the thermal compensation system are present. Baffles for stray light mitigation systems are also visible. Credit: The Virgo Collaboration.

An active control of the entire suspension is needed to suppress the effects of ground motion below 2 Hz, since they are amplified by the resonance modes of the suspension structure. A hierarchical control strategy is adopted: very low-frequency mirror oscillations below 10 mHz, like the ones given by Earth tides, are compensated for by a system of coil-magnet actuators from the top of the inverted pendulum. Then residual motion at the level of the payload is reduced by the action of the reference mass on the marionette. Finally, nanometer scale motion is controlled at the mirror level by the reference mass acting on small magnets bonded to the mirror surface.

The latest measurement of the Advanced Virgo SA performance shows attenuation values below 10^{-10} above 10 Hz [100], proving that the SA is effective in reducing seismic noise in the detection band well beyond the Advanced Virgo requirements, both for vertical and horizontal motion.

Thermal noise (payload and mirror suspension): in the frequency region from a few Hz to 30 Hz the major limit to the detector sensitivity is given by the mechanical thermal noise of the mirror suspension wires. Following the fluctuation-dissipation theorem [101], the thermal noise power spectral density of a mechanical system is proportional to its energy dissipation, which is quantified by the loss angle parameter defined as:

$$\phi = \frac{1}{2\pi} \frac{E_{\text{dissipated per cycle}}}{E_{\text{stored}}} \quad (1)$$

Materials with low mechanical losses must be chosen in building mirror and suspension, and all the possible sources of dissipation must be taken into account and minimized in assembling the system together. Fused silica is the key material for advanced detector realization. Excellent optical and mechanical properties, and easy machining make fused silica the natural choice to build the GW detector mirror substrates. Moreover, since fused silica offers a loss angle which is four orders of magnitude smaller than the best steel [102,103], and a breaking strength which is twice higher [104], fused silica fibers are also used in core mirrors suspension in an almost monolithic configuration. After some pioneering tests [105–107], a monolithic suspension has been realized for the first time to suspend the ≈ 6 kg mirrors of the GW detector GEO 600 [108,109], and then for building the ≈ 21 kg mirrors suspension of the first Virgo upgrade, named Virgo+ [110]. Currently, 42 kg mirrors are suspended by four fused silica fibers both in Advanced LIGO [111] and Advanced Virgo [98].

Virgo fibers are produced by a 200 W CO₂ laser pulling machine, using a feed and pull technique [112,113]. Fibers have a diameter of 400 μm and a length of 700 mm determined as the distance between the two bending points, placed at the mirror and marionette center of mass, respectively [114]. The fiber diameter and length are designed to confine the violin modes at frequencies above 400 Hz, and the vertical modes below 10 Hz. Geometric and elastic fiber parameters are accurately measured and the repeatability is good enough to allow for mirror positioning within a residual inclination of less than 1 mrad.

Immediately after production, fibers are completely pristine, and their measured mean breaking strength is about 4 GPa, more than four times higher than the working load. Unfortunately, silica is a very fragile material and any improper handling can produce micro-cracks which result in an abrupt reduction of the fiber strength and an unavoidable suspension failure. The fiber ends are welded to two silica pieces specifically designed to be bonded to the marionette at the upper extremity, and to the mirror at the lower one. Figure 6 shows the lower part of the fibers attached to the mirror.



Figure 6. Mirror suspension of fused silica fibers. Two fibers are welded to rectangular silica pieces anchored to another silica rectangular block which in turn is attached to flats worked out in the mirror lateral surface. All the silica surfaces are attached by hydroxide-catalysis bonding. Credit: The Virgo Collaboration.

In the low frequency band (<40 Hz) most of the elastic energy is stored close to the fiber ends, meaning that those are the regions where the energy losses must be minimized. A thicker profile of the fiber ends (800 μm in diameter), is expressly designed for reducing thermo-elastic dissipation, i.e., the energy loss due to heat production and diffusion during the fiber elastic bending [115]. The welding quality, attained using the laser pulling machine, makes dissipation in this region negligible. The bonding between mirror and marionette is realized by hydroxide-catalysis bond technique, applied to $\lambda/10$ polished surfaces [107,116,117]. This technique allows for low energy losses, by getting very thin

bonding layers (less than 100 nm). Direct measurements show that the current Advanced Virgo configuration suspension thermal noise is mainly due to marionette recoil losses. Nevertheless, this is not an impediment to the fulfilling of the required specifications, such losses being overcome by the radiation pressure [98].

4.2.2. Mid-Frequency: Optics & Coatings

In the frequency band from 30 Hz to 300 Hz, the detector sensitivity is limited by the thermal noise of the coating layers deposited on the core mirror surfaces, in order to achieve the right value of reflectivity. Advanced Virgo and Advanced LIGO core mirrors are large cylinders of ultra-pure fused silica (Suprasil™3002 and 312), with a diameter of 350 mm, a thickness of 200 mm, and a weight of 42 kg [82]. This kind of material is highly transparent to 1064 nm laser light (absorption is less than 0.3 ppm/cm for Suprasil™3002), and also exhibits an extremely low value of the loss angle ($\phi \approx 10^{-9}$). The ultra-fine polishing of the mirror surfaces achieves sub-nanometric roughness, limiting scattered light and possible asymmetry in optical losses between cavities. Reflectivity is assured by a coating film applied to the mirror surfaces by ion beam sputtering (IBS) [118]. The coating is made by a stack of alternate layers of two materials with different refractive indexes, forming a Bragg reflector, and it is deposited with a residual roughness of the same level of the polished substrate (≈ 0.5 nm). Coating power absorption is lower than 1 ppm, and the reflectivity of the end mirror is 99.999% [119].

The energy losses of a system composed by different parts can be computed as the sum of the loss angles of each part, weighted by the energy stored in that part. For the mirrors, the coating loss angle is much larger than the substrate one, hence, even if the energy stored in the thick substrate is larger, coating is responsible for most of the energy losses, and consequently for the resulting thermal noise [120,121]. For advanced detectors, silica (SiO_2) is used as low refractive index material, whereas titania doped tantala ($\text{TiO}_2:\text{Ta}_2\text{O}_5$) is used in Advanced Virgo and Advanced LIGO and pure titania (Ta_2O_5) in KAGRA as high refractive index material [119,122]. A post-deposition thermal treatment (annealing) for a time duration of 10 h at 500 °C is done after coating deposition to lower optical absorption and internal stress. This treatment also improves the mechanical properties of the coating reducing the loss angles of the whole stack [123,124]. After annealing, IBS deposited silica shows a mechanical loss angle of $2.2 \cdot 10^{-5}$ at 60 Hz, which is about three to four order of magnitude larger than the silica bulk loss, but still considerably smaller than the loss angle of tantala ($2.8 \cdot 10^{-4}$ at 60 Hz). Doping tantala with titania (with a ratio $\text{Ti}/\text{Ta} = 0.27$) decreases the loss angle of about 25% ($2.2 \cdot 10^{-4}$ at 60 Hz), still ten times above the silica one [125]. This makes the mid-frequency sensitivity of current detectors limited by the thermal noise of the high refractive index layers of coating. By means of an optimization process [126] a tuning of the coating layers on the stack has been done in order to ensure the right value of reflectivity using the minimum total thickness of high index layers. Nevertheless, finding a new high index material exhibiting the same optical characteristic of $\text{TiO}_2:\text{Ta}_2\text{O}_5$ and lower mechanical losses, is mandatory for increasing the detector performance [127].

4.2.3. High Frequency: Laser & Squeezing

At high frequencies, Advanced Virgo is affected by photon shot noise. This is one of the components of quantum noise, arising from vacuum fluctuations, associated with the lowest quantum state of the electro-magnetic field, which enters the dark port of the interferometer and interacts with the main beam. The frequency-dependent response of the detector allows distinguishing between two different components of this noise. In fact, at frequencies below 100 Hz, the detector senses *radiation pressure noise*, while at higher frequencies it senses *photon shot noise*. The first, being hidden by technical noises, did not affect the sensitivity of Advanced Virgo.

High power laser: in order to reduce shot noise and then improve the sensitivity of the detector over 100 Hz, a higher input power has been employed. The input beam is

provided by a system that ensure stable power, frequency and beam pointing [82]. The laser system is able to provide around 200 W of laser power as an input for the Input Mode Cleaner (see Section 4.1). The requirements are: frequency fluctuations less than a few $\mu\text{Hz}/\sqrt{\text{Hz}}$, power fluctuations of the order of $10^{-9}\sqrt{\text{Hz}}$, beam pointing less than $10^{-11}\text{rad}\sqrt{\text{Hz}}$.

Such a stable high power is obtained through several steps. A commercial 1 W Nd:YAG laser is connected to two amplifiers each providing a beam with a power of 100 W, using single mode polarization maintaining fibers. The two beams are then coherently added in order to have a unique laser beam. The frequency is first prestabilized using a Reference Cavity in order to obtain a laser linewidth less than 1 Hz; then, the stabilization is further increased, in steps, first using the Input Mode Cleaner cavity and then, during the lock acquisition procedure (see Section 4.3.1), the arm cavities of the interferometer itself. This chain forms a multi-stage servo loop that uses piezo-transducer of the master laser as actuator. The power laser fluctuations are compared to a stable voltage, and the obtained error signal is used to control the power stability by acting on the high power amplifier pumping diode current. To distinguish these fluctuations from other disturbances, the photodiode providing such signal is placed under vacuum after the Input Mode Cleaner. Moreover, in order to control the shape and the beam pointing of the laser, a Pre-Mode Cleaner (PMC) cavity, placed on the same bench as the main laser, is used. This cavity has a finesse of 500 and is placed in a horizontal plane; for this reason, it reduces the horizontal beam jitter. Although these systems would have allowed reaching up to 175 W transmitted by the Input Mode Cleaner, it has been decided to inject less power, also to reduce parametric instabilities due to the excitation of the internal acoustic modes of the test masses that can overlap with optical higher order modes in which the light can be scattered. This coupling can contribute to the amplification of the mechanical motion of the test masses.

Frequency Independent Squeezing in Advanced Virgo: during O3, much of the improvement of the Advanced Virgo sensitivity was also due to the injection of squeezed vacuum states. These states are characterized by correlated amplitude and phase uncertainties, and their interaction with the interferometer beam contributes to the reduction of quantum noise. In this section, a description of the apparatus used for squeezed vacuum production and injection in Advanced Virgo will be described. This apparatus is basically composed by an external bench where a squeezing vacuum source, provided by the Max Planck Institute for Gravitational Physics (AEI [128]), and all the optics useful for the injection are hosted.

The squeezed vacuum source, located on a 1 m^2 breadboard, is based on a down-conversion nonlinear process occurring in an Optical Parametric Oscillator (OPO). This consists of a Periodically Poled Potassium Titanyl Phosphate (PPKTP) non-linear crystal with a curved and high reflection coated back surface and an external coupling mirror. This cavity is pumped by a 532 nm beam in turn produced by a Nd:YAG laser operated at 1064 nm, in the following referred as squeezer main laser, through a Second Harmonic Generation (SHG) process using a similar nonlinear cavity working in up-conversion mode. A small Mach Zehnder interferometer, with controlled arm length, is used for the pump power stabilization. The squeezer main laser also provides a local oscillator beam that will be used as reference for the measurement of the produced level of squeezing before the injection in the interferometer, using a balanced homodyne detector. Finally, a triangular cavity is used as mode cleaner and as frequency and polarization filter for this beam. The length of all the cavities present in the squeezer are controlled using the Pound-Drever-Hall (PDH) technique [129,130] and an active control stabilizes the temperature of the non-linear crystals contained in the OPO and SHG cavities within the mK range. To produce squeezed states at the frequencies of interest for gravitational wave detectors, a coherent control technique, described in [131], has been used. For this purpose, a 500 mW Nd:YAG auxiliary laser is used, by shifting it in frequency with respect to the main laser by 7 MHz, using a

phase-locked loop (PLL). Another PLL is used to make sure that the squeezer main laser and the interferometer input laser have the same frequency [132,133].

The shape of the squeezing beam is matched with the one of the interferometer using a mode matching telescope which is totally reflective and it is made by curved mirrors; this allows minimizing the optical losses, which would decrease the squeezing level. The distance between them can be tuned using micrometric screws. Moreover, an off-axis geometry has been chosen to compensate for astigmatism. The back-scattered light, coming from the interferometer, is drastically limited using a chain of three Faraday Isolators. Finally, two tip-tilt actuated steering mirrors and a further Faraday Isolator are used to inject the squeezing through the gravitational wave detector output port. The injection of phase-squeezed vacuum states inside the interferometer brought to the reduction of shot noise, which dominates the high frequency part of the detection band, by a factor of about 3 dB [134].

4.3. Interferometer Operation

In Section 4.1 the description of the optical layout of Virgo was addressed, together with its principle of operation. Given the very strict operating conditions, due to the necessity of near-perfect destructive interference, and the presence of several resonant optical cavities within the detector, it is clear that the acquisition, control and tuning of the detector's working point are of paramount importance: the acquisition and control of the main optics, of both their longitudinal position and angular orientation, is done via the *Global Controls*, which then interact with the *Thermal Compensation System*, the purpose of which is to optimize the optical parameters of the main optics; together, they define the optimal working point of the interferometer.

4.3.1. Global Controls

The working point of the interferometer is defined by the destructive interference condition of the central Michelson, and the resonance condition of the several resonant cavities of the detector. This translates in the definition of several longitudinal degrees of freedom (DOF), based on the relative position of the main optics, which are the following, considering the BS mirror as the origin of the coordinate system (cf. Figure 2):

- $MICH = l_N - l_W$, it is the length difference of the short arms of the Michelson, and it defines the interference condition;
- $PRCL = l_{PR} + \frac{l_N + l_W}{2}$, it is the length of the Power Recycling cavity;
- $CARM = \frac{l_N + l_W}{2}$, it is the average, common arm length of the long Fabry-Pérot cavities;
- $DARM = l_N - l_W$, it is the differential arm length of the long Fabry-Pérot cavities; this degree of freedom is sensitive to the strain induced by the passage of a gravitational wave, so it is the most important of all and it ultimately determines the sensitivity of the interferometer.

Each of these DOFs has to be controlled with high accuracy, in order to bring, and then keep, the interferometer in its correct working point. This is achieved by means of a serial procedure, called *lock acquisition*, during which the control of the DOFs are engaged one after the other, exploiting several optical configurations which ease such acquisition; once all of them are controlled, the working point is adiabatically brought to the one needed for science observation.

The main technique used for the control of the longitudinal DOFs is the Pound-Drever-Hall (PDH) technique [129,130], which is based on the phase modulation of the carrier light at several radio frequencies; such modulation, performed by the EOM (cf. Section 4.1), generates several sidebands which are resonant or anti-resonant in the different cavities of the interferometer. Then, the field probed by different photodiodes placed in several ports of the detector are demodulated at the same radio frequencies, in order to provide viable error signals which are used in feedback control loops, which actuate on one or more optics each (see Figure 2).

The mirrors need not only to be controlled in longitudinal position, but also in angular orientation; this already happens when the interferometer is not locked, when each mirror is controlled in angle independently one from the others using optical levers, a *local control* provided by a Superluminescent Diode (SLED), which impinges on the mirror and then is focused on a Position Sensing Device (PSD). However, this type of control has a lower accuracy with respect to the needed requirement for science operation and, in addition, is ground-based so it can only provide a local reference and not a global one from the interferometer point of view.

Therefore, during the lock acquisition sequence, such control is replaced with an angular *global control* scheme, based on error signals provided by quadrant photodiodes (QPD), which are displaced in the same suspended benches as the longitudinal PDs and therefore provide a global reference.

However, once the interferometer is progressively locked, effects induced by radiation pressure arise and make the control scheme more complex; for the two recycling cavities such effects are negligible, so that the angular DOFs of the involved mirrors remain decoupled. On the other hand, the radiation pressure effects are quite strong inside the long Fabry-Pérot arm cavities, and they induce an optical spring between the cavity mirrors. To diagonalize the sensing, a description of the DOFs in a *common/differential* basis is more apt. Such a description can be viewed in Figure 7, with the following definitions:

- COMM(+): common tilt of the arm cavities: the effect is two beams recombining in the same spot on the BS mirror;
- DIFF(+): differential tilt of the arm cavities: the effect is two spots recombining on the two opposite sides of the BS mirror;
- COMM(−): common shift of the arm cavities: the effect is two beams recombining in the same spot on the BS mirror;
- DIFF(−): differential shift of the arm cavities: the effect is two spots recombining on the two opposite sides of the BS mirror.

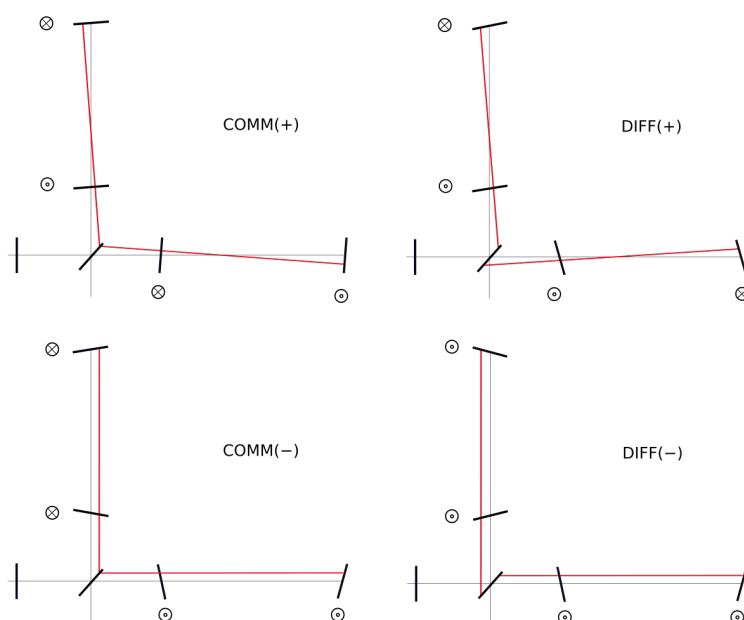


Figure 7. Scheme of the angular DOFs of the Fabry-Pérot arm cavities.

Such a scheme allows a complete control of the orientation of the optics up to the required accuracy for the working point of the interferometer, which is of the order of magnitude of hundreds of nrad for the two (−) modes, tens of nrad for the PR and BS mirrors while for the (+) modes, which are the most critical ones, it is as high as a few nrad [135,136].

For a more detailed description of the control and noise subtraction techniques used in Advanced Virgo, additional information can be found in [137–139].

4.3.2. Thermal Compensation System

The increase of the laser input power, useful to reduce the shot noise, introduces thermal effects and optical aberrations due to the power absorption of the mirrors. To restore the working point of the detector, a thermal compensation system is needed.

Thermal effects are one of the principal sources of wavefront distortion for the laser beam circulating into the interferometer. For a beam transmitted from an optic, they can change the optical path length due to *thermal lensing*, *thermo-elastic deformations* and *elasto-optic effects*. In the case of fused silica, only the first component contributes to wavefront distortion [140]. While, for a reflected beam, thermo-elastic deformations of the mirror surface impact on the wavefront due to a bump that appears in the center of the mirror. The mirrors of the interferometer are not all affected by the same thermal effects: despite all the mirrors absorbing light, in both the high reflecting face and substrate, thermal lensing must be corrected only for the input mirrors of each Fabry-Pérot cavity. In fact, the substrates of the power recycling mirror and of the end mirrors are not inside the cavities of the detector: for these mirrors, only the coated part impacts on the shape of the circulating beam. Thermal lensing in the input test masses degrades the shape of the beam and influences the gain of the sidebands in the power recycling cavity which, being a marginally stable cavity, becomes difficult to control. Moreover, the deformation of the radius of curvature of all the mirrors introduces higher order modes resonating inside the cavities.

Wavefront distortions contribute to the decrease of detector sensitivity and the reduction of the stability and the robustness of the detector; for this reason, a Thermal Compensation System (TCS) has been realized for Advanced Virgo. This is an optical system that senses the wavefront distortions and dynamically corrects them using suitable actuators. The sensing and actuating systems will be described in the following.

The TCS sensing apparatus is constituted by a series of Hartmann Wavefront Sensor (HWS), designed at the University of Adelaide [141] and fully characterized at the University of Rome Tor Vergata [142]. The main components of this sensor are a *charge coupled device* (CCD) and a *Hartmann Plate* (HP), which contains an array of holes. The sensor works by computing the difference between the wavefront of a beam that experiences aberrations and a reference one produced by a *superluminescent light emitting diode* (SLED) with a wavelength of 780 nm. The reference beam is reflected back by the mirror under test impinges on the HP, along the same path. If this beam is distorted, the pattern recorded on the CCD reveals a displacement with respect to the spot left by the reference beam and the wavefront variation is computed. The optical path variation due to thermal effects in the two input masses is sensed using an *on-axis measurement*, while the thermo-elastic deformation of the HR surfaces of all the other mirrors is sensed with *off-axis measurement*. The first procedure is useful to monitor thermal lensing in the power recycling cavity. For this reason, for each input test mass, two HWSs are used, one in the injection area and the other in the detection area. The one used for the West Input test mass is located on the External Injection Bench (EIB), where the Advanced Virgo main laser is located; the one used for the North Input test mass is located on the External Detection Bench (EDB). The second procedure, used to sense the thermo-elastic deformation, is performed using one HWS for input and end test masses, each one located on a dedicated bench near the corresponding tower.

Another device, the *phase-camera*, developed by the Nikhef group, is used for an indirect sensing and it is complementary to the HWS, with the difference that it provides a global sensing without distinguishing between the different optics. On the other hand, this device is able to measure the amplitude of a beam and it is able to distinguish the contribution of fields with different frequency. This means that this can give information about the carrier and the signal. The maps of the phase-camera are obtained by comparing

the beam under test with a reference beam, which is a pick-off of the main laser taken before it enters the interferometer, and therefore free from aberrations. In Advanced Virgo, two of these devices are used, one in reflection from the power recycling cavity, in order to monitor the aberrations of the beam inside it, and another in correspondence to the dark port.

The actuation part of the TCS is used for a dynamical correction of the deformations sensed by the sensing system. In particular, thermo-elastic deformations, due to the power absorption of the coatings, are corrected using *ring-heaters* around each mirror. A ring-heater is composed by two parallel heaters and a shield.

The thermal lensing is corrected using a CO₂ projector. This is constituted by a CO₂ laser beam that shines the mirror with an annular pattern in order to compensate the temperature gradient due to the Gaussian transversal distribution of the main laser light. In Virgo this annular pattern was done by shining the CO₂ laser beam on an axicon, which is a conic lens, with the pattern that directly heats the mirror; instead in Advanced Virgo, due to the more stringent requirements on the laser fluctuations, it shines an additional transmissive optic, called *compensation plate*.

The optical systems that allow to have the right patterns for each test mass are located on dedicated benches and it can work in three different configurations, depending on the pattern the laser beam will show: *central heating*, *double axicon system* and *scanning system*. The first is a Gaussian beam shined on the center of the compensation plate and it is used when the interferometer laser is off in order to avoid thermal transients. Due to the possibility to change its dimensions, this will be used also for other purposes that are described in [143,144]. The second configuration provides the annular pattern. While in Virgo this was provided by a single axicon, in Advanced Virgo, due to the stricter requirements on the residual aberrations, it is provided by two concentric annuli, one small and thick, the other larger and thinner. The last configuration is devoted to the corrections of the non-symmetric wavefront distortions on the input test mass due, for example, to the non-uniform absorption. It consists in scanning the mirror point by point and sending the suitable heating pattern locally on the CP with galvo mirrors.

5. Performance of the Advanced Virgo Detector in the O3 Observing Run

The infrastructure choices, the technological developments, the accuracy of the controls and the determination of the working point of the interferometer are ultimately all devoted to the same purpose, which is to contribute to the performance and the stability of the detector. This has two important aspects to be considered: the capability of the instrument to measure the physical effect of interest with a good sensitivity, and the quality and reliability of the data itself taken by the detector. In this section both these aspects will be addressed regarding the O3 Observing Run, with a focus on the evolution of the performance of the Advanced Virgo detector in recent years, the comparison between the LIGO and Virgo performance and the contribution of the latter to the performance of the GW detector network as a whole.

5.1. Noise and Performance in O3

The performance of the detector can be pinned down to one characteristic figure of merit, the *sensitivity curve*, from which the performance in terms of observing capability of specific benchmark sources at a given distance, the *range*, can be derived.

As was previously stated in Section 1, a gravitational-wave interferometer such as Advanced Virgo is tasked to measure the passage of a gravitational wave, i.e., the *strain* $h(t)$ induced by it. As is clear from Section 4.2 the response of the detector is frequency dependent, so the usual description of the performance is by means of the sensitivity curve $h(f)$, which is depicted in Figure 8. In the Figure, the evolution of the sensitivity of the Advanced Virgo detector can be observed, from the one obtained in the O2 Run to the latest one of the second part of the O3 Run, O3b: the performance of the Virgo detector is in line with the design sensitivity for such Run, as shown by the comparison with the

Observing Scenario target reported in [145], and it is improved by a factor 2 with respect to the previous O2 Run [139].

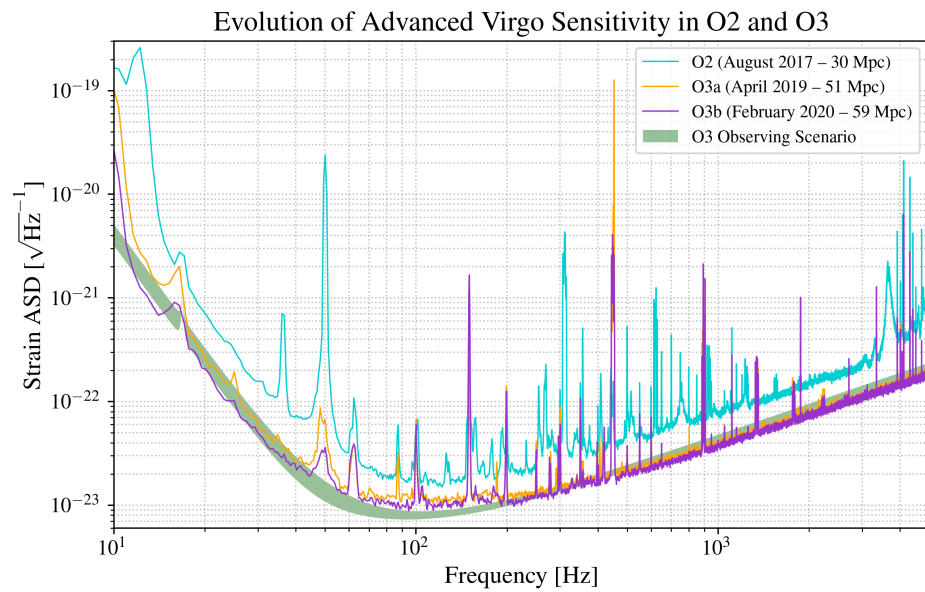


Figure 8. Evolution of the sensitivity curve $h(f)$ of the Advanced Virgo detector in its Observing Runs, and comparison to the design sensitivity for Virgo (Observing Scenario [145]).

The sensitivity curve is a comprehensive description of the overall performance of the detector, as a function of frequency; however, astrophysical studies show particular and definite types of expected sources of gravitational waves, which are distinct in terms of amplitude, frequency and shape of the expected gravitational wave signal. Such parameterized sources constitute *benchmark sources*, which can translate the sensitivity curve information in a single number, which is the distance, or *Range*, at which an interferometer is sensitive to. The most used benchmark sources are Binary Neutron Star (NS-NS) and Binary Black Hole (BH-BH) systems, which were described in Section 2.

In terms of NS-NS Range ¹ (the most widely used), Advanced Virgo during the O3 Run peaked at 60 Mpc, which was set as the target sensitivity for the Run, with a steady Range of 59 Mpc during the second part of the Run, O3b; this is twice the sensitivity that was reached in the previous O2 Run in August 2017. The overall performance of the HLV Network is represented in Figure 9.

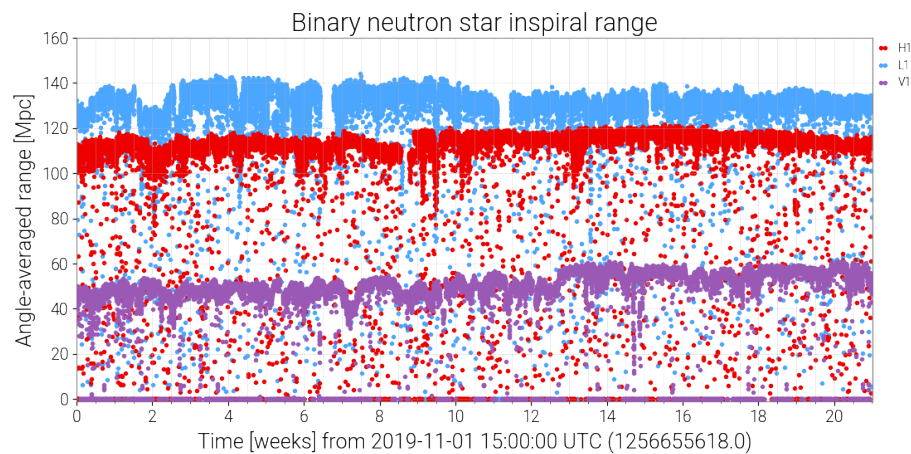


Figure 9. NS-NS Ranges of the HLV Network (LIGO Hanford—LIGO Livingston—Virgo) during the O3b Run. Image from [147].

While the sensitivity curve and the range speak of the absolute performance of the detector, also the *duty cycle* is of paramount importance, as the stability of the detector, and therefore its capability to be stably online in Science Mode directly affects the probability of a detection, and the number of them; moreover, since bringing the interferometer to Science Mode (the *lock acquisition* procedure, see Section 4.3.1) is a lengthy procedure, reducing the number of times it is needed to acquire the lock directly affects the duty cycle. As it can be seen in Figure 10 the duty cycle of Advanced Virgo in O3b has been quite high, as around 76 % of time was spent in Science Mode; most of the downtime is due to scheduled activities, like Commissioning shifts and the weekly Maintenance and Calibration shifts, while only around 13 % of time has been spent in lock acquisition and detector troubleshooting.

This achievement, together with the performance of the two LIGO detectors [148], allowed also the global network duty cycle to be high. In Figure 10 there is the overall duty cycle of the HLV network in the O3b Observing Run: the percentage of observing time when all three detectors were online was of about 51 %; this is the best working condition for the interferometer network, as it guarantees a higher SNR for the detections and a much better capability of locating the source and its distance. Still, joint detections are possible also with two detectors online simultaneously, and the overall fraction of the O3 Run in such a condition was 34 % of the time. Only 15 % of the Run had only one or zero detectors locked and in Science Mode, which is proof of a good network performance, considering each detector’s necessary and scheduled downtime for Maintenance and other side activities.

The importance of a high network duty cycle resides in the fact that not only it obviously increases the probability of the detection of a GW event but, maybe more importantly, having three detectors online at the same time greatly increases the capability of the network in localizing the source of the GW event, which is something of paramount importance especially in the case of GW event with an EM counterpart, as for example the NS-NS events (as GW170817 [85]) (see for example Section 6.3.3). Another important reason for having a high network duty cycle is for the detection of continuous signals, which of course benefits from long datasets. For all these reasons, although in terms of absolute sensitivity the Virgo contribution is improving only marginally the overall network sensitivity in terms of strain $h(f)$ or *Range*, its contribution in terms of localization and network duty cycle has been very important.

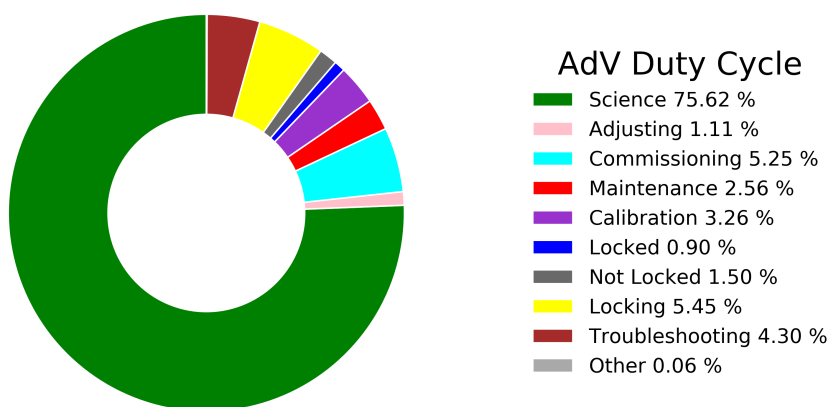


Figure 10. Cont.

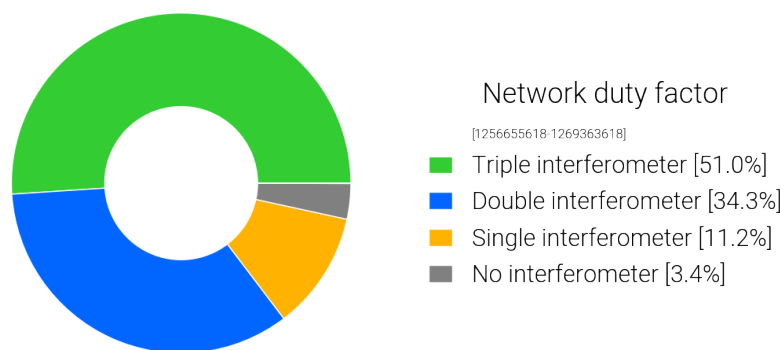


Figure 10. Top: Duty cycle of Advanced Virgo during O3b. **Bottom:** Duty cycle of the Gravitational Waves Network of the three Advanced detectors Virgo (V1), LIGO Livingston (L1) and LIGO Hanford (H1) during O3b. Bottom image from [147].

5.2. Data Quality

The final aim of the detector monitoring and characterization activities is to provide information about the noise in the detector and its environment to identify and mitigate disturbances and improve the detector sensitivity. This is especially useful before the actual data taking e.g., during commissioning phases, where the detector’s status and performance are continuously monitored, and in preparation for future runs. On the other hand, an effort is also necessary to improve search sensitivities during the run, in this step the collaboration with the data analysis groups is fundamental [149,150]. For the reasons listed above, a data quality model for Advanced Virgo is necessary. Data quality products should be delivered to the different data analysis groups. Some of these are commonly shared between the groups, while some others should be adapted, e.g., for online and/or offline searches.

One of the most important data quality products is the list of the “science” segments, i.e., the collection of GPS times validated to be used for actual GW searches. For example, during data taking, the measured strain is reconstructed online as $h(t)$. Monitoring tools are used to flag the data as good or bad as it can happen, for example, that the detector undergoes to a lock “loss”, which invalidates the data for the analysis. The collection of all the data taking periods for which the detector is not considered “safe” enough to do science are categorized as “Online CAT1” vetos. During O3, only 0.18% of Virgo data were labeled as CAT1 [151].

The second class of activities which is more directed to data analysis groups, as we have said, aims to improve search sensitivities. Data quality products needed for transients searches (e.g., Bursts/CBC) differ from those used for the search of persistent signals (e.g., CW and stochastic). Typically, short-duration noise events, known as glitches, affect mostly the first category of searches, while spectral features, known as lines, can mimic the presence of a persistent signal. It is worth saying that both noise sources are not optimal if present in the vicinity of any GW signal. Tailored tools, optimized for the rejection of specific time-frequency regions according to the search performed, are used for this scope. The noise investigation is performed also using the information provided by auxiliary data channels, including environmental sensors and human inputs when needed.

For transients GW detection, in particular for CBC events which are the only type of signal detected so far, the test to assess the data quality of a signal have been automatized in the data quality report (DQR). Indeed, for each alert produced by the Gravitational-Wave Candidate Event Database (GraceDb) [152] a DQR page is provided, listing all the possible sources of noise concerning the event. To be validated, a GW event should pass a series of tests and the noise background should not present particular features which can pollute

or blind the event. In addition to the pure data/noise quality tests, the environmental conditions of the detector at the time of the alert are also controlled. Among others, the following are checked: data quality flags (e.g., if the detector is in Science Mode, cf. Section 5.1); the glitch and spectral noise characterization in the time and frequency regions of the event; the Virgo state vector, a data acquisition channel used to define good data for online analysis pipelines.

In addition to transient GW events validations, information from tools for the identification of spectral noise features, known as lines, are also provided to data analysis groups. There are persistent lines that are present during the full run, such as the main power line at 50 Hz, transient lines that are present only during a short period and even those that wander in frequency during the run. Some of these lines, which are strong enough and last for a good fraction of the run are clearly visible in the spectrum as upwards peaks above the noise floor, see Figure 8 or 13. Most of these lines are identified looking at the data from auxiliary environmental channels, while others are collected during the final stages of the searches for persistent signals when final candidates need to be eventually validated or excluded.

6. Data Analysis and Results

Whenever searching for signals with a known waveform buried inside a noisy time series, the matched-filter theory [153] is a well-established methodology. Therefore, CBC sources (for which we have an overall precise description of the waveform as a function of its physical and extrinsic parameters) have been mostly searched for with various implementations of that technique. Matched-filter algorithms are also used for the search of known pulsars.

Modeled searches: searches for well-modeled sources of GWs typically use matched-filter-based algorithms, where a waveform model is correlated with data over the detectors' sensitive bands to extract signals from detector noise. Though matched-filter algorithms are optimal just in the case of known signal waveforms embedded in Gaussian stationary noise, they are unparalleled in many cases, such as, e.g., when dealing with the detection of compact binary signals for which the signal energy is spread over a long time interval. Examples of matched-filter pipelines for CBC searches include *gstLAL* [154], *PyCBC* [155] and the Virgo developed *MBTA* [156]: those pipelines are used both on low-latency mode and off-line on archival data. For CW searches for known pulsars, matched-filter approach is adopted mainly by the *5-vector* [157,158] method, *F/G statistic* [159,160], time-domain heterodyne-based pipelines (*Bayesian and Band-Sampled-Data*) [161–163]. In this case, the investigated parameter space is significantly narrower when compared with a full all-sky search or with directed searches. For those, the number of templates needed to cover the full parameter space can quickly become impractical. This is the main reason semi-coherent methods have been developed, where chunks of data are first analyzed coherently (e.g., using matched-filter) and then combined incoherently. CW searches using semi-coherent methods, where the typical GW frequency evolution of a source is given by its Taylor expansion in time, include the *Frequency Hough* [164], the *Sky Hough* [165], *Weave* [166], *Power Flux* [167], *TwoSpect Algorithm* [168].

However, for other GW sources such as, e.g., CCSN, matched-filter algorithms are hardly viable: though we have some estimates on the energetics, the expected waveforms are a stochastic superposition of the specific processes occurring at the collapse. More in general, a detected signal waveform from a known source (e.g. with an EM or neutrino counterpart) could be significantly different from model predictions or, alternatively, a fully unexpected source might be emitting GW signals. In all the above-mentioned cases, unmodeled algorithms are to be preferred.

Unmodeled searches: those are generic searches, designed to detect a wider class of GWs. For short transients (i.e., \lesssim of a few seconds), such approach relies mostly on coherent excess-power methods [169,170], where the data power is coherently summed over regions of the time-frequency domain looking for local excesses, and/or on applying

minimal assumptions on the signal morphology (e.g., frequency, duration, polarization, etc.). Given the lack of waveform model constraints and the presence of noise transients, signal coherence over two or more GW detectors is usually a crucial feature of any unmodeled GW transient candidate. Such algorithms are also being used for CBC searches as they are robust with respect to a variety of features including higher multipoles, high mass ratios, misaligned spins, eccentric orbits and possible deviations from general relativity, which may create mismatches between signal waveforms and simulated CBC templates. Examples of unmodeled GW transient pipelines include, coherent WaveBurst (cWB) [171,172] (which is used both in low-latency and off-line on archival data), oLIB [173] and X-Pipeline [174]. For the case of long-lasting or persisting signals, for which fast noise transients are less of a concern and no particular assumption on the signal model is done *a priori*, semi-coherent or incoherent methods can be used, these include Viterbi [175], the Sidereal Filter [176] and cross-correlation based-methods such as CrossCorr [177], STAMP [178] or Radiometer [179]. Typically, these methods are also applied in low-mass X-ray binary searches such as Sco-X1 [180,181] and others [182].

Following the identification of a GW candidate by a search pipeline, parameter estimation allows one to estimate the potential properties of the event. Such follow-up studies provide for a better understanding of the signal consistency and are a crucial part of the vetting of GW candidates.

Parameter estimation and sky localization: as gravitational waveforms directly encode crucial information about the source's intrinsic (e.g., the masses and spins for compact objects) and extrinsic (e.g., arrival times, a constant phase, source location, etc.) parameters, recovering such physical parameters from the GW observations is a key analysis task. Bayesian inference is the leading methodology which is used to infer the sources' astrophysical properties from GW data. Multiple Bayesian stochastic sampling tools, implementing different sampling techniques, such as Markov chain Monte Carlo [183,184] and Nested sampling [185], have been developed and are currently used: within the CBC tools, the most widely used are LAL INFERENCE [186], BILBY [187] and PyCBC INFERENCE [188]. While stochastic sampling methods for full GW parameter estimation can take hours or more to converge, prompt sky localization pipelines, such as BAYESTAR [189] and cWB [190] take just tens of seconds to produce probability sky maps that are comparable in accuracy to the full analysis, i.e., allowing searches for electromagnetic counterparts. Finally, the unmodeled waveform reconstruction is performed with BayesWave [191,192] and cWB.

6.1. All-Sky GW Searches

All-sky and all-times searches (also known as untriggered) analyze all available GW data with no assumption on the GW signal incoming direction and time of arrival. Untriggered, all-sky searches have the greatest potential of finding EM dark sources and, potentially, to discover unexpected sources. They also provide triggers for follow-up studies of candidate events with EM observations. There are indeed many "all-sky" GW searches, each one adopting different methodologies (as briefly described in the previous section): they can be, somewhat arbitrarily, grouped in two main families, the modeled and unmodeled all-sky searches.

To the first group belong the modeled searches, i.e., those performed with matched-filter pipelines. For the CBC case, the highest significant and more outstanding GW events have been published both in dedicated papers and in GW catalogs, while the other detections and a small fraction of the marginal triggers are published in catalogs only. The main results produced by these searches will be resumed in Section 6.3. As it happens in many other fields/contexts which use matched filtering, the signal is not known exactly. For compact binaries, the theoretical waveform models (i.e., templates) from the inspiral, merger and ringdown phases of such systems depends on many *a priori* unknown parameters. An optimized grid of templates covering the parameter space at a fixed minimal match has to be devised for these searches. To limit the number of templates, i.e., the computational load of the search, a trade-off needs to be found between

the reduction of the considered parameter space (neglecting, e.g., precession, higher order modes, eccentricity, etc.) and minimizing the detection losses. In that context, algorithms for template placement play a crucial role. The same happens for the all-sky searches for CWs, where the intrinsic parameters, namely the frequency and the time derivative of the frequency, plus the source sky position, span a wider range of values with respect to the CBC searches. Additionally, in this case, no *a priori* assumption is made. CW all-sky searches are typically less sensitive and more computationally intensive than those for known pulsars where fewer templates are used for the search.

To the second group belong all the generic untargeted searches for GW transients, such as, e.g., the searches for burst signals targeting a wide class of short duration (i.e., \lesssim a few seconds) generic bursts [193,194] and long duration (i.e., with a duration between a few tens and a few hundred seconds) generic bursts [195,196], i.e., the most “agnostic” searches, devised to capture the unexpected unknowns. The unmodeled pipelines also contributed to the detection and analysis of BH-BH events published in the LIGO-Virgo Catalogs [4,5] and to the LIGO-Virgo electromagnetic follow-up program [197], with BH-BH and intermediate-mass black hole binaries dedicated all-sky searches.

6.2. Multi-Messenger Searches

Multi-messenger searches of transient sources can be divided into two main categories: EM and neutrino follow-up of candidate GW signals and externally triggered GW searches.

In the first scenario, low-latency GW searches provide fast alerts to the astronomical community in order to allow the prompt EM and neutrino follow-up of candidate GW signals. As mentioned before, several automatic low-latency GW data analysis pipelines have been built to continuously monitor the GW data and search for transient GW signals; these pipelines are able to detect candidate GW events within a few seconds, and GW candidates are stored in GraceDb. Immediately after one of the search pipelines reports a GW event, sky localization and parameter estimation analyses begin. If candidates are significant enough (i.e., if their False Alarm Rate is below a fixed threshold) and pass some automated data quality checks (“automated vetting”), they are shared with the astronomical community through the Gamma ray Coordinates Network (GCN) protocol, consisting of machine-readable Notices plus short bulletins (Circulars) with human descriptions of the events. During O1 and O2 the LIGO/Virgo GCN network was private: messages were sent only to astronomers who signed a Memorandum of Understanding (MoU) with the LIGO and Virgo collaborations, with a latency of ~ 20 –1000 min (see, e.g., [197]).

During O3, the GW alerts were public² and the latency was shorter: a first preliminary GCN notice was automatically sent out for the GW candidates that satisfied pre-established criteria, with a typical time delay of the order of minutes.

After this, a Rapid Response Team (RRT), composed of researchers from the detector sites, the analysis teams, the detector characterization team and the low-latency EM follow-up team, and chaired by the run coordinator, had to confirm or retract the candidate on the basis of semi-automated detector characterization and data quality checks (this phase is called “human vetting”, see also Section 5.2); for the confirmed GW candidate an Initial notice and circular were issued, otherwise a Retraction notice and circular were sent out. The Initial and Retraction notices/circulars were typically issued within a few hours from the GW trigger; Update GCN notices and circulars were also issued if further analysis led to improved estimates of the sky localization, of the source classification or of the significance accuracy. For a schematic view of the Alert timeline, see Figure 11.

In the second scenario, GW searches are triggered by the detection of an EM or a neutrino event. This is the case, for instance, of GW searches triggered by GRBs, in which GW data are analyzed in detail to find a possible GW signal in temporal and spatial coincidence with a GRB; this kind of search has the advantage to significantly reduce the detection threshold due to known time and sky location of the source (see, e.g., [198]). In the case of GRBs two search methods are used: a modeled search for binary merger signals associated with short or ambiguous GRBs, and an unmodeled search for GWs associated

with all GRBs (both long and short). The modeled search looks for a GW signal compatible with the inspiral of a binary system containing at least one NS within 6 s of data associated with an observed short GRB; the analysis is done with a coherent matched filtered pipeline, PyGRB [199,200], which is part of the general open-source software PyCBC [155] and has core elements in the LALSuite software library LALSuite [201]. For the unmodeled searches, the analysis is carried out with the X-Pipeline software package [174,202]. X-Pipeline looks for excess power that is coherent across the network of GW detectors and consistent with the sky localization and time window for each GRB; the search time interval begins 600 s before the GRB trigger time and ends either 60 s after it, or at the T_{90} ³ if it is larger. The above described time windows are based on the expected time delay between the GW signal and the EM signal.

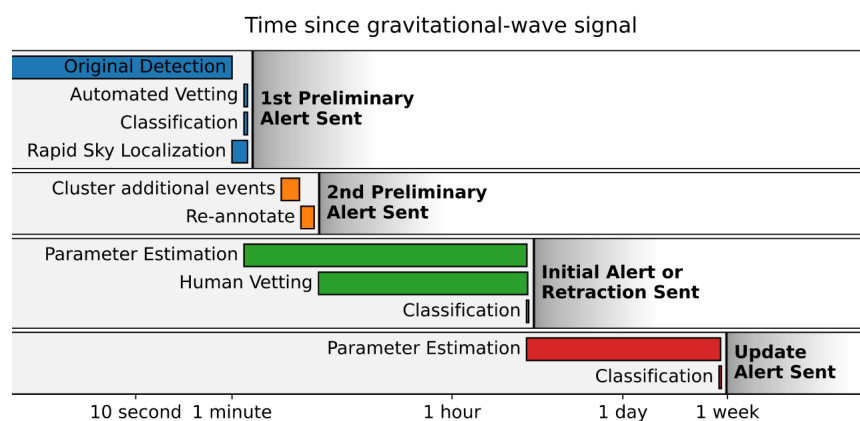


Figure 11. Alert timeline for O3. Image credit: Public alerts User Guide, <https://emfollow.docs.ligo.org/userguide/index.html> (accessed on 10 August 2021).

In addition to this, there are several online pipelines that perform low-latency searches of coincidences between EM events or neutrino event candidates and GW triggers. Specifically, the Rapid On-Source VOEvent Coincidence Monitor (RAVEN, [203]) process alerts for GRBs from both *Fermi*-GBM and the Neil Gehrels *Swift* Observatory [204], as well as galactic supernova alerts from the SNEWS⁴ collaboration and looks for coincidences in time between these events and the GW triggers recorded in low-latency (that may not be significant enough on their own). The Low-Latency Algorithm for Multi-messenger Astrophysics (LLAMA, [205]) combines instead GW triggers with High Energy Neutrino (HEN) triggers from IceCube.

Information provided by astronomers can also be used for other scopes in addition to low-latency searches. In the context of searches for persistent signals, EM information is used to constrain the investigated parameter space. For example, source catalogs such as the latest *Fermi*-LAT one [206] can be used to identify new CW candidates, such as supernova remnants potentially hosting a NS, for which directed searches are typically performed [34–36] using fully coherent or semi-coherent methods. The synergy in this field is twofold: EM information is crucial to limit the parameter space to investigate but, on the other hand, the detection of GWs from a particularly interesting sky region, could be a trigger for astronomers for the observation of new populations of compact objects. In fact, a widely studied case, where this latter aspect is fundamental, is the search for GWs (mainly CW and stochastic) from the Galactic Center [37,207]. The detection of a GW emission from this region, if due to the presence of a pulsar population, can potentially solve the origin of the GeV excess measured by gamma-ray telescopes [208,209], debated to be due to dark matter around Sgr A* [210].

6.3. Results

Since the first direct detection of GWs from a merging BH-BH system in 2015 (GW150914 [83]), 50 signals from CBCs have been published so far by the LIGO and

Virgo Collaborations. The most comprehensive publications on these signals are the two Gravitational-Wave Transient Catalogs ⁵: the first catalog release, GWTC-1 [4], reports 11 detections made during Advanced LIGO and Advanced Virgo's first and second Observing Runs, including 10 signals from BH-BH coalescences as well as the first signal from a binary neutron star (NS-NS) coalescence, GW170817 [85], which was also the first joint detection of gravitational waves and electromagnetic radiation (see Section 6.3.3); the second catalog release, GWTC-2 [5], adds 39 detections observed during the first part of the third Observing Run (O3a), including the second signal from a NS-NS, GW190425 [211] (see also Section 6.3.3), two signals from CBCs with very asymmetric component masses, i.e., GW190412 [212] and GW190814 [213] (see also Section 6.3.2), and a signal from the merger of two heavy BHs that formed an intermediate-mass BH (GW190521, [214]).

The impact of these discoveries also includes fundamental physics, astrophysics and cosmology, as we are finally probing gravity in the strong-field regime, constraining neutron-star matter equation of state and Hubble constant and directly measuring coalescing binaries population parameters. Typically, CBC signals, especially high-mass events, can also be used to investigate lensing effects. Results on O3a data [215] are consistent with the expected low rate of lensing at current detector sensitivities, including the contribution from non-observation of the SGWB from BH-BHs and NS-NS events.

In the following, we will report the main LIGO-Virgo scientific results from the last 5 years, with a focus on the detections of CBCs (Sections 6.3.1–6.3.3), the testing of deviations from GR (Section 6.3.4) and, finally, on the upper-limits on persistent signals (Section 6.3.5) and cosmic strings (Section 6.3.7).

6.3.1. BH-BH/IMBH Detections

Thanks to the increased number of BH-BH mergers observed through GWs, some properties of the BH-BH population have been better understood [216]. For instance, it has been possible to obtain insight into the BH-BH primary mass spectrum: it is not well described by a power-law with a sharp high-mass cut-off; there is instead a strong statistical preference for other models with non-trivial features such as a peak or a tapering occurring at $\sim 37 M_{\odot}$, where pair instability SN (and pulsational pair-instability SN) is expected to shape the mass distribution of BHs. Furthermore, a fraction of the detected BH-BHs have component spins whose orientation is anti-aligned with respect to the orbital angular momentum of the binary; under the assumption that such systems can only be formed by dynamical interaction, this may imply that BH-BHs observed by Advanced LIGO and Advanced Virgo can merge both dynamically and in the field. Finally, the increased statistics allowed us to put new constraints on the BH-BH merger rate density, estimated to be $\mathcal{R}_{\text{BH-BH}} = 23.9^{+14.3}_{-8.6} \text{ Gpc}^{-3} \text{ yr}^{-1}$. As already mentioned (see Section 2), stellar mass BH-BH mergers are not expected to have EM counterparts, although a possible optical counterpart has recently been reported in association with GW190521 [10].

6.3.2. NS-BH Detections

During the second half of the third Observing Run of Advanced LIGO and Advanced Virgo (O3b), there was the observation of GW signals from two CBC inspiral which are consistent with NS-BH binaries: GW200105 and GW200115 [217]. These discoveries represent the first confident observations to date of NS-BH binaries via any observational means. Considering only these two events, the NS-BH merger rate density has been estimated to be $\mathcal{R}_{\text{NS-BH}} = 45^{+75}_{-33} \text{ Gpc}^{-3} \text{ yr}^{-1}$; when adding also less significant search-triggers with masses consistent with the typical range associated with NS-BH binaries, we have $\mathcal{R}_{\text{NS-BH}} = 130^{+112}_{-69} \text{ Gpc}^{-3} \text{ yr}^{-1}$. No EM counterpart has been observed so far in association with GW200105 and GW200115.

Besides these two events, there are other two candidate events observed during O3a that may have originated from a NS-BH or a BH-BH merger: GW190426_152155 and GW190814 [5,213]. GW190426_152155 was the GW candidate event with the highest false alarm rate in O3a, and therefore it could be a detector noise artifact; GW190814 is consistent

with the coalescence of a binary system whose first component has a mass consistent with a BH, while the secondary component has a mass in the mass gap between known NSs and BHs: it could be therefore either the lightest BH or the heaviest NS known to be in a CBC system [213]. No EM counterpart has been observed for these events (see, e.g., [218,219]).

6.3.3. NS-NS Detections and EM Counterparts

On August 17th, 2017, at 12:41:04 UTC, a NS-NS inspiral signal (GW170817) was observed by Advanced LIGO and Advanced Virgo [85]. Less than two seconds later (~ 1.7 s), a short GRB (GRB 170817A) was detected by two space-based instruments: the Gamma-ray Burst Monitor (GBM) onboard the *Fermi* satellite [220], and the spectrometer anti-coincidence shield (SPI-ACS) onboard INTEGRAL [221]. This joint detection marked the birth of multi-messenger astronomy with GWs and provided the first direct evidence that at least a fraction of NS-NS mergers are progenitors of short GRBs [222]. Furthermore, the observed time delay between GRB170817A and GW170817 allowed us to put constraints on the difference between the speed of gravity and the speed of light, estimated to be between -3×10^{-15} and $+7 \times 10^{-16}$ times the speed of light [222].

An extensive EM follow-up campaign was performed after this joint detection, especially after the release of a three-detector, well constrained GW skymap (see Figure 12), with a 90% credible region of only 31 deg^2 [223]. This campaign led to the discovery of an optical transient (SSS17a/AT 2017gfo) in the host galaxy NGC 4993, located at a distance of ~ 40 Mpc, less than 11 hours after the merger [224]; such counterpart was also detected in ultraviolet and infrared wavelengths (see [223] and references therein). Photometric and spectroscopic observations of the source allowed to identify it as a kilonova [225,226]: this supports the hypothesis that NS-NS mergers are sites of r-process nucleosynthesis of heavy elements.

Several days after the NS-NS merger, an X-ray [227] and a radio [228] counterparts were also discovered. The evolution of the X-ray and radio light curves, together with the unusual low gamma-ray luminosity of GRB 170817A, suggested two possible scenarios: an off-axis GRB with a relativistic, structured jet or a “cocoon” emission from the relativistic jet shocking its surrounding non-relativistic material [222]; thanks to subsequent very long baseline interferometry observations it has been possible to constrain the size of the source and its displacement: these were found to be consistent with a structured, relativistic jet [229,230].

The above described multi-messenger observations allowed to use GW170817 as a standard siren, the GW analog of an astronomical standard candle, to measure the Hubble constant H_0 [231]. This measurement is independent of other state-of-the-art measurements of H_0 , and in particular, independent of the cosmic distance ladder used to calibrate standardizable sources such as type Ia supernovae (see, e.g., [232]): in fact, the GW analysis can be used to estimate the luminosity distance directly, without the use of intermediate astronomical distance measurements. Combining the luminosity distance of GW170817 inferred with GW data and the recession velocity of NGC 4993 inferred with electromagnetic data, H_0 has been estimated to be $70_{-8.0}^{+12.0} \text{ km s}^{-1} \text{ Mpc}^{-1}$ [231]: this value is consistent with previous, independent measurements [233,234]. This first multi-messenger event including GWs clearly demonstrates the potential for cosmological inference from GW standard sirens. In the future, we expect to have more multi-messenger NS-NS detections, and the combination of subsequent independent measurements of H_0 from these standard sirens will lead to an era of precision GW cosmology.

NS-NS mergers can also be used to test the structure of cold, ultra-light density matter [235]. Neutron star interior can reach values above the nuclear saturation density, ranking them among the most dense objects known in the Universe. This peculiar property makes the study of the internal structure and the physical processes happening inside these unique objects impossible to replicate with experiments on Earth. The gravitational wave event GW170817 represents the first attempt to constraint the EOS of NS with GWs. The tidal deformation of the companion begins just before the merger; in this phase and

during the ringdown of the remnant, the GW signal carries important information of the deformability of the star and hence on the properties of the matter composing the object. In the companion paper of the detection of GW170817 [235] it has been possible to determine the radii of the involved objects in the range between 9 km to 13 km, while the measure of small values of the tidal deformability parameter suggests that “soft” EOSs are favored over “stiff” EOSs.

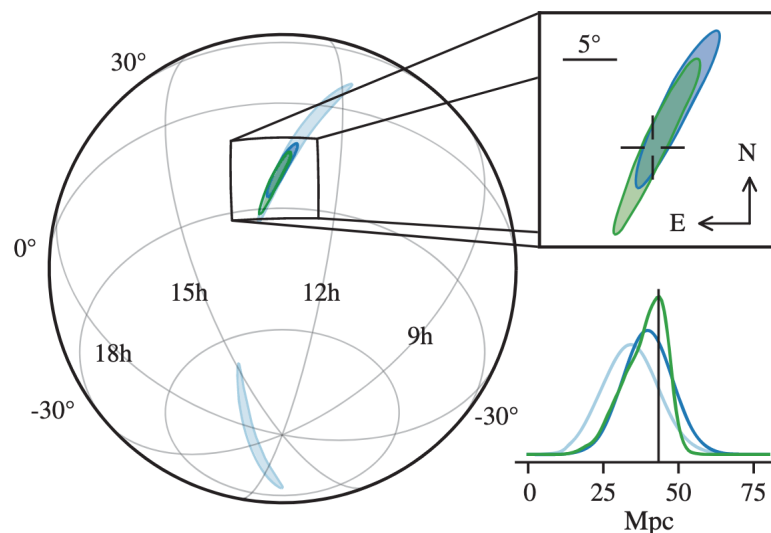


Figure 12. Sky location reconstructed for GW170817 by a rapid localization algorithm from a two-detector (LIGO Hanford and LIGO Livingston, 190 deg^2 , light blue contours) and a three-detector (LIGO Hanford, LIGO Livingston and Virgo, 31 deg^2 , dark blue contours) analysis. A higher latency three-detector analysis improved the localization (28 deg^2 , green contours). In the top-right inset panel, the reticle marks the position of the host galaxy NGC 4993. The bottom-right panel shows the a posteriori luminosity distance distribution from the three gravitational-wave localization analyses. The distance of NGC 4993 is shown with a vertical line. Figure from [85]; © The Authors, published by the American Physical Society. This is an open access article distributed under the terms of the Creative Commons Attribution License 4.0 (<http://creativecommons.org/licenses/by/4.0/>) (accessed on 10 August 2021)).

Besides GW170817, another potential NS-NS merger has been observed during the third Observing Run of Advanced LIGO and Advanced Virgo: GW190425 [211]. The masses of the two components of the binary are in the range expected for NSs; however, both the source-frame chirp mass and the total mass of the system are significantly larger than those of Galactic NS-NS systems: this might be an indication that GW190425 formed differently than known double NSs in our Galaxy. No EM counterpart has been observed in association with this event (see, e.g., [218]). The detection of GW170817 and GW190425 allowed to constrain the NS-NS merger rate density to be $\mathcal{R}_{\text{NS-NS}} = 320^{+490}_{-240} \text{ Gpc}^{-3} \text{ yr}^{-1}$ [216]

6.3.4. Tests of GR

GW observations can be used to check for deviations from general relativity theory also in the strong-field regime. These tests include the limits on the graviton mass, consistency of the detections with Kerr BH-like signals, possible dispersion in the propagation of the GW. So far, no evidence of new physics has been achieved. To test GR with GW detection of compact objects, where velocities reach a fraction of the speed of light and curvatures of the spacetime are large, both accurate numerical relativity simulations and high post-Newtonian order calculations are needed. The latest result using the most significant CBC signals detected so far and reported within the second Gravitational-Wave Transient Catalog (GWTC-2) [5] are reported in [236]. Given the difficulty to produce waveforms directly derived from non-GR theories, the results of [236] can only be interpreted

as constraints on deviations from GR derived from the detections during the first two Observing Runs of Advanced LIGO and Advanced Virgo (O1, O2) and the events detected in the first half of the third Observing Run (O3a). An attempt to interpret those results as effects of non-GR theories are given in [237,238]. Mainly two aspects were tested in [236], consistency of GR predictions and the study of specific deviations from GR. In addition to these, other properties of the wave have been considered for additional tests, including the terms from the spin-induced quadrupole moment of the binary components, the study of the ringdown and echoes phases of the remnants and checks on the GW polarizations. In the paper, no evidence for deviations from GR has been found, improving previous constraints [239] by a factor ~ 2 . No evidence for GW dispersion, tightening previous constraints on Lorentz-violating dispersion parameters by a factor of ~ 2.6 , and constraints on the mass of the graviton as $m_g \leq 1.76 \times 10^{-23} \text{ eV}/c^2$ at 90% confidence level have been placed. Concerning the properties of the remnant, all are consistent with Kerr remnant and no GW echoes, which could reflect extra structures near the event horizon not present for classical BHs, have been found. Studies on GW polarizations with three detectors can only test the nature of purely scalar or purely vector polarization versus the pure tensor case expected for GR. Also in this case, no evidence for non-tensor GWs has been found.

6.3.5. Persistent Signals in O3

Among the most sensitive searches for persistent signals, in particular for the search of CW from isolated neutron stars, known pulsar searches reach the maximum sensitivity depth. As already mentioned, these searches strongly rely on the EM information available about the source.

Indeed, ephemerides from NICER [240] have been used to place constraints on the gravitational wave emission from the X-ray energetic pulsar PSR J0537-6910 [31]. Amplitude upper limits improve existing results by a factor of up to 3, placing stringent constraints on theoretical models for r-mode driven spin-down in PSR J0537-6910. Additionally, a search for GW emission at both once and twice the rotational frequency (i.e., for emission due to “mountains”) for the same target with LIGO and Virgo O2 and O3 data are given in [33]. No CW signal has been detected in this search but, for the first time, the spin-down limit⁶ for this type of emission on this source has been surpassed. From reported numbers, gravitational waves from the $l = m = 2$ mode contribute to less than 14% of the spin-down energy budget. Latest results for five radio pulsars, comprising three recycled milliseconds pulsars (PSR J0437-4715, PSR J0711-6830, and PSR J0737-3039A) and two young pulsars, the Crab pulsar (J0534+2200) and the Vela pulsar (J0835-4510), are reported in [32]. Results from this work constrain the equatorial ellipticities of some of the targets to be less than 10^{-8} , i.e., well below the expected theoretical maximum values.

In the context of directed searches, the latest results from the search of fifteen supernova remnants are reported in [34]. In this search, three search pipelines with distinct signal models and methods of identifying noise artifacts have been used. The strain upper-limit reach values as low as $\sim 8 \times 10^{-26}$ for the most sensitive pipeline, and it slightly improves the previous constraints set by [36] on the closest target (Vela Jr.), despite the use of a coherent integration duration ~ 20 times shorter.

Finally, the latest LVC results for all-sky searches for GWs from isolated NSs [241] report upper limits on the strain for the most favorable orientation of 6.3×10^{-26} using early O3 data, improving previous results from O2 data [38]. Results for searches of unknown neutron stars in binary systems, spanning orbital periods of 3–45 days, are reported in [39] where upper limits on the strain are placed at 2.4×10^{-25} . All-sky searches have also been performed by external groups, reporting results on publicly released O2 data in [242–245]. Results for searches using the full O3 dataset are in progress.

Another kind of persistent signals are those forming the SGWB. For the case of isotropic stochastic searches, mainly based on cross-correlation methods, upper limits derived from the first three Observing Runs are given in [246]. Since the results of the search are consistent with uncorrelated noise, upper limits on the dimensionless energy

density are reported, improving previous bounds by a factor of 6.0 for the flat background case. No evidence for gravitational waves in any of the three analyses in [207] looking for the anisotropic SGWB has been found. Hence, 95% confidence-level upper limits on the gravitational-wave energy density due to extended sources on the sky, on gravitational-wave energy flux from different directions on the sky, and on the median strain amplitude from possible sources in the directions of Scorpius X-1, the Galactic center, and SN 1987A are reported. Direction-dependent upper limits on the gravitational-wave emission improve upon existing limits by a factor bigger than 2.0.

6.3.6. Dark Matter

The search of DM with interferometric detectors is a relatively new field explored by the collaboration. We briefly review the main results achieved for these searches. The effects of superradiance around black holes as potential emitters of CWs have been investigated in [247]. In this work, for the first time, direct constraints on the ultra-light scalar boson field mass forming clouds around spinning black holes have been placed. A range of boson masses, roughly $(1.1 \times 10^{-13} - 4 \times 10^{-13})$ eV for high initial black hole spin, and $(1.2 \times 10^{-13} - 1.8 \times 10^{-13})$ eV for moderate spin, have been excluded with strong confidence. Boson clouds around spinning black holes could also alter the parameter estimation of the mass and the spin of BH-BH events by a quantity dependent on the scalar boson mass. Using the GWTC-2 events of LIGO and Virgo, the authors in [248] find that the existence of scalar bosons in the mass range between 1.3×10^{-13} eV and 2.7×10^{-13} eV is strongly disfavoured. An attempt to look for DM candidates using CBC events has been done in [249], where the GW190521 event could have been produced not by the standard merger of a pair of black holes, but could be due to the merger of two head-on collisions proca stars i.e., bosons stars constituted by ultra-light vector boson particles with masses of $8.72_{-0.82}^{+0.73} \times 10^{-13}$ eV. In [250] upper limits on the coupling constant have been placed using LIGO and Virgo data: these surpass the ones provided by existing dark matter experiments, such as the Eöt-Wash torsion balance and MICROSCOPE. This result also improves the one reported in [251] using LIGO O1 data.

6.3.7. Cosmic Strings

Cosmic strings are theoretical objects possibly formed in the early Universe [252]. These objects, formed by cusps and/or kinks, could have been left over after a phase transition of the early Universe [253] and when interacting they can form loops, either through the overlap of a string with itself or when it encounters another string in the cosmic string network. So far there is no clear evidence for their existence, and results from the cosmic microwave background (CMB) experiments ruled out a significant contribution from cosmic string to the background. Another way to detect these line-like topological defects is to look for the gravitational wave emission produced when these objects oscillate. For instance, after a loop is formed, it oscillates and radiates energy also through the emission of gravitational waves [254–256]. The expected signal in this case could be, occasionally, a powerful burst arising from the background, mainly produced by cusps and kinks on the string; more often the global sum of single and lower burst signals form an un-resolvable noise background, the stochastic GW background. The latest attempt to look for GW signals produced by cusps, kinks and kink-kink collisions has been done using the full O3 Run data of LIGO and Virgo [257], using three different models of cosmic string loop distribution. Although no detection for single short-duration transient signals has been found, constraints on the cosmic string tension $G\mu$ have been derived from the SGWB energy density upper limits [246]. These constraints on the tension $G\mu$, as a function of the number of kinks per oscillation, of the Nambu-Goto strings, derived for different cosmic string loop distribution models, improve previous results in [258–260] by up to 2 orders of magnitudes. For the one-loop distribution model, the upper limit on the tension $G\mu \leq 4 \times 10^{-15}$ is the most stringent present in literature. Furthermore, the results in [257] for strings formed at the end of the inflationary era in grand unified theories, are

not completely in agreement with the simple inflationary models; this leaves the floor to questions about the need for extra fields able to obstacle the formation of cosmic strings.

7. Future Prospects for Advanced Virgo Plus

After the conclusion of the O3 run, many changes have started to be implemented in the Advanced detectors to increase their sensitivity. The upgrading work of Advanced Virgo is divided in two phases [261]. The installation of the Phase I upgrades has already completed and currently commissioning is ongoing to reach the target sensitivity by the beginning of the O4 run that is foreseen to start around the middle of 2022. These changes involve many aspects of the detector. The major contributions to the improvement of the sensitivity will come from an increment of the laser power at the source, the installation of a signal recycling cavity, and the implementation of a frequency dependent squeezing technique. Phase II upgrades will be installed during the break between O4 and O5, but several R&Ds are currently ongoing to finalize the configuration of all the detector subsystems and the installation procedures. Major changes foreseen in Phase II are: an enlargement of the beam size at the end mirrors, an increment of the mass of the end mirror up to 105 kg, a new high reflective coating of the core optics.

7.1. AdV+ Phase I: The Upgrades for the Next Observing Run

Frequency Dependent Squeezing: one of the main goals for the improvement of the sensitivity in view of the next Observing Run (O4) is a broadband quantum noise reduction. The frequency independent squeezing used in Advanced Virgo will be no more effective. In fact, due to the reduction of low-frequency technical noises and the increase of the power circulating into the interferometer, the low frequency component of the quantum noise, the radiation pressure noise, will also limit the detector sensitivity. To do this, a frequency-dependent squeezing technique will be used. This technique is based on the dispersion properties of a detuned filter cavity. Experiments performed starting from 2005 confirmed the effectiveness of this technique and recent experiments demonstrate its feasibility at the frequencies of interest for gravitational wave detectors [262–266]. The choice made for Advanced Virgo Plus is to use a 285 m long linear cavity with a Finesse of about 11000, this will allow to have a squeezing angle rotation at 25 Hz that is the frequency below which the interferometer sensitivity will be radiation pressure noise limited. The two cavity mirrors have a diameter of 15 cm and a radius of curvature of about 558 m that can be corrected using a ring heater placed around each of them.

To have this detuning, the cavity must be locked using an external laser frequency shifted with respect to the frequency of the squeezed beam. This laser, called Sub-Carrier, will be aligned on the squeezing cavity. Its frequency shift will ensure that it will be completely reflected back from this cavity. A good mode-matching with the cavity ensures that this beam will be well overlapped with the squeezing beam up to the filter cavity. Another beam with a frequency of 532 nm at which the filter cavity has a lower Finesse, about 100, will be used for first alignment and easier lock. The experience gained during O3 drove many of the technical choices done for the design of the injection system, mostly to avoid possible issues due to optical losses and obtain a 7 dB to 8 dB of shot noise reduction without affecting the low-frequency sensitivity [267]. To do this, totally reflective and motorized telescopes will be used along the path of the squeezed beam. Moreover, low-loss Faraday Isolators will be used for the injection of frequency-independent squeezing towards the filter cavity and for the injection of the frequency-dependent squeezing from the cavity to the interferometer. The loss reduction will be also helped by the new Output Mode Cleaner of the interferometer. The two OMCs used in Advanced Virgo (see Section 4.1) are replaced with a unique OMC with a much higher Finesse. Having one OMC instead of two will avoid the losses due to the mode matching between the two mode cleaner cavities.

The installation of the frequency-dependent squeezing system is in progress. The squeezed vacuum source, located on an in-air bench, is the same as for O3 with minor modifications made. On the same bench, an external homodyne detector is placed in order

to have the possibility to measure and characterize the squeezing without interfering with the commissioning of the interferometer. The beam coming from this bench will reach two suspended in-vacuum benches linked by a 12 m long in-vacuum pipe. The first suspended bench contains a double-stage Faraday isolator used for the injection of the frequency independent squeezed vacuum states toward the filter cavity and the frequency-dependent squeezed states, coming from the cavity, towards the interferometer, passing through another low-loss mode matching telescope. In addition to other optical elements, it also contains one of the mirrors of a further mode-matching telescope, while the other one is placed on the other suspended bench. The second suspended bench is linked to the filter cavity input mirror by another in-vacuum pipe with a length of 40 m [261].

Signal Recycling Cavity and Auxiliary Laser System: as anticipated in Sections 4.1 and 5.1, the Advanced Virgo Detector did not have a Signal Recycling mirror up to the O3b run, and it was replaced by a simple lens. For the forthcoming O4 run such semi-reflective mirror will be installed: this will create another resonant cavity inside the interferometer, the Signal Recycling Cavity (SRC). Because of the optical layout of the interferometer, this SRC is made by the SR mirror itself and by the two arm cavities as a whole, effectively adding one longitudinal degree of freedom, the Signal Recycling Cavity Length (SRCL), to the already existing ensemble.

The key point about this additional cavity is its *tunable* nature: the working point of this cavity can be chosen, as a microscopic tuning ϕ of the SRCL working point, depending on the desired outcome on the detector sensitivity. Given the geometry of the interferometer, the SR mirror basically forms, together with the ITMs and the ETMs, a double cavity SRM-ITM-ETM; the ETM in particular sees the ensemble SRM-ITM as a compound mirror, with a reflectivity which depends on the SRCL working point; this ultimately changes the Finesse of this double cavity. The possible configurations are the following:

- **broadband configuration:** the Signal Recycling Cavity has a detuning $\phi = 0$; both the carrier and the sidebands are resonant in the SRC; the Reflectivity of the compound mirror is high, so the cavity Finesse is high and the cavity pole is moved to lower frequencies;
- **tuned configuration:** the Signal Recycling Cavity has a detuning $\phi = \frac{\pi}{2}$; the carrier is not resonant in the SRC, while the sidebands are; the Reflectivity of the compound mirror is low, so the cavity Finesse is low and the cavity pole is moved to higher frequencies;
- **detuned configuration:** the Signal Recycling Cavity is in an intermediate configuration, where $0 \leq \phi \leq \frac{\pi}{2}$; here there is a single frequency where the detuning is equal to the round trip phase, resulting in a peaked response of the interferometer at a single frequency.

For Advanced Virgo Plus the foreseen configuration is the *tuned* configuration.

In any case, the presence of this additional resonant cavity makes the lock acquisition procedure more difficult with respect to the previous one, and poses a significant challenge about acquiring control of all the longitudinal degrees of freedom at the same time. For this reason the choice was made to change the lock acquisition scheme in favor of a more innovative one, based on an additional Auxiliary Laser System (ALS), composed by an additional beam injected in the interferometer, at double the frequency of the main one, which is used in order to acquire control of the arm cavities and then bring them out of resonance with respect to the main laser. Then, the central part of the interferometer can be locked on the usual main beam; finally, the arm cavities are adiabatically brought back to the main laser's resonance and finally the control is switched from the auxiliary laser to the main one, and the five longitudinal degrees of freedom are all controlled with the main laser and the interferometer is locked as a whole.

This kind of approach has been studied extensively [268,269] and is already in operation in both the LIGO [270] and KAGRA [271] interferometers; the Virgo implementation is slightly different and has been studied and developed as reported in [272].

7.2. AdV+ Phase II: Towards the Limit of the 2nd Generation Detectors

A second, more drastic upgrade of the detector will happen at the end of O4, when important changes will involve different detector subsystems [261]. In addition to a further increment of the laser power, and a consequent improvement of the scattered light mitigation system, the most relevant changes will be the new heavier and larger end mirrors. Increasing the mirror weight from the current 42 kg to 105 kg corresponds to a reduction in radiation pressure. Enlarging the mirror diameter from 350 mm to 550 mm makes it possible to increase the width of the laser beam, which has a positive impact on thermal noise as it will be explained below. In Figure 13 the foreseen detector sensitivity evolution in the next runs is shown [145].

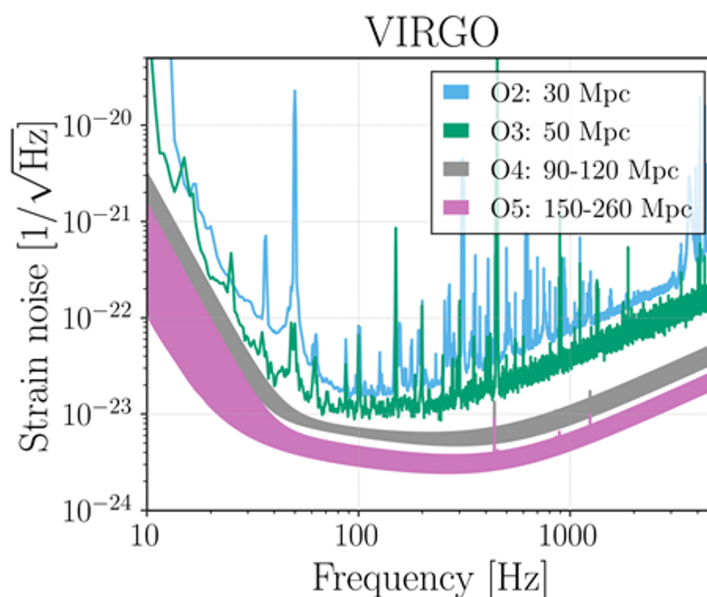


Figure 13. The evolution of the Advanced Virgo sensitivity in the past two Observing Runs, and the expected sensitivity for the next two. Advanced Virgo Plus Phase I will run in O4, while the Phase II upgrades will be implemented between O4 and O5. Figure from [145]: © The Authors, published by Springer Nature. This is an open access article distributed under the terms of the Creative Commons Attribution License 4.0 (<http://creativecommons.org/licenses/by/4.0/> (accessed on 10 August 2021)).

Impact of large masses in AdV+ subsystems: adopting heavier mirrors has a considerable impact on many different detector subsystems. The payload has been completely redesigned to host the new test mass. A design prescription is to maintain the same overall mass of mirror, marionette and cage, so that only small adjustments are needed on the Superattenuators. The new payload must contain the new baffles for stray light control and the elements of the thermal compensation system adapted for the heavier mirrors and larger beams. The payload design has been recently finalized and a first prototype is currently being produced. The suspension silica fiber design has been modified to meet the new working loads [113]. To keep the same value of working stress as in the lighter mass configuration (800 MPa), the fiber thickness has been increased from 400 μm to 640 μm . In this way also the frequencies of bouncing and violin modes remain unchanged. Regarding fiber reliability, even though some studies indicate a reduction of the fiber strength as the diameter increases, first tests show a breaking stress still more than three times higher than the working load. Nevertheless, the stress imposed to the silica pieces welded to the fibers, and to the bonding surfaces, increases with the mirror size, hence an accurate design of those parts with the help of finite element analysis has been done.

New coating performance: since the detector sensitivity is limited by the coating thermal noise, the main issue is to find a new coating recipe comparable with the current

one in terms of optical proprieties (absorption and scattering), but with significantly lower thermal noise. The Virgo Coating R&D Collaboration (VCR&D) has been established between many groups already involved in the Virgo project with the aim of conducting coating research [127,273], and within the LIGO Collaboration a very active parallel research is progressing. There are different ways to reduce coating thermal noise, which can be written as in [274]:

$$S_x(f) \propto \frac{Td}{w^2} \left(\frac{Y_C}{Y_S} + \frac{Y_S}{Y_C} \right) \phi_C \quad , \quad (2)$$

where the Young moduli of coating (Y_C) and substrate (Y_S) appear in a combination which is minimized for $Y_C = Y_S$. Equation (2) shows that barring a cryogenic solution (with low temperature T), coating thermal noise is reduced by enlarging the beam width (w), and reducing the coating thickness (d) or the coating loss angle (ϕ_C). The large mirrors that will be installed as end test masses in Advanced Virgo Plus make possible the enlarging of the beam size, even if extending the deposition area without spoiling the coating quality is a technological challenge. Consequently, a huge effort in coordinating the coating research of both LIGO and Virgo Collaborations is devoted to obtain the best possible coating recipe soon enough to leave time for the technological development of the deposition process. The plan for the coating research is based on three different kinds of activities:

- synthesis of new materials, new deposition techniques and new post deposition treatments
- optical, structural and mechanical characterization of the synthesized products
- modeling of the static and dynamic behavior.

Following this research scheme, many results were achieved, such as a better knowledge of the mechanical dissipation mechanisms [275], also by means of molecular-dynamic simulations [276], a deeper understanding of the role of annealing and doping processes [122,123], and the important discovery of a link between mechanical losses and absorption [277]. Nevertheless, the main target of the research is to find a new material for replacing titania doped tantala in high refractive index layers of the coating stack. Currently, a couple of very promising materials are under study, with the aim of optimizing the deposition parameters, while a huge effort for obtaining a complete characterization is also ongoing.

8. Conclusions

This paper presented an overall picture of the current status of the Virgo experiment, focusing on the Advanced Virgo project, which took place for the O2 and the O3 Observing Runs. The scientific reason of this endeavour has been made clear by defining the scientific goals and achievements that this kind of experiment could make possible; the description of the long timeline GW experimental science went through in the last decades served as both an important historical introduction and as a hint of the many struggles and technological techniques that have been pursued in order to explore the possibility of the detection of GWs. A more focused attention has been put on the Italian history of experimental GW science, which spanned from the initial resonant bars detectors to the more advanced laser interferometric techniques. The joint effort of France and Italy put the foundation of the Virgo Collaboration, which ultimately led to the construction and operation of the largest and more sensitive European laser interferometer devoted to GW science. After several decades of technological advancements, the Advanced Virgo project ultimately brought the Virgo detector to its first detection of gravitational waves in 2017, joining the LIGO detectors at the end of the O2 Observing Run. The end of such run also marked the beginning of the multi-messenger astronomy era, as the LIGO and Virgo detectors jointly detected the first GW signal from a NS-NS system, which was followed by the detection of EM counterparts from other experiments, in a coordinated effort. The International Gravitational Waves Network (IGWN) then participated concurrently to the following O3 Run, which saw a substantial increase in the detection rates, thanks to the improved sensitivities of the detectors. This state of the art of the Advanced Virgo detector in the O3

era was thoroughly discussed in both its main features, as in the most recent developments of the instrument, as well as the latest improvements in data analysis and validation. Finally, a short description of the already ongoing improvements for the next future of the Virgo detector has been provided, in view of the next Observing Runs, where the Advanced Virgo Plus project will carry forward the capabilities of this 2nd generation detector for the next years to follow. At the same time, the other interferometers of the IGWN, i.e., the LIGOs and KAGRA, are undergoing similar upgrading stages, each detector targeting its own design sensitivity [145]. The final aim of these upgrades is to widen the astrophysical reach of the detector and to drive below the sensitivity curve for the case of nearby sources. Along with these detectors improvements, data analysis groups are constantly updating the search pipelines in order to be ready to analyze data for the upcoming O4 run. In the meantime, data from the O3 run is being analyzed in the case of long-lasting signals, and further results from transient searches are in preparation.

Funding: This research received no external funding.

Acknowledgments: The authors gratefully acknowledge the Italian Istituto Nazionale di Fisica Nucleare (INFN), the French Centre National de la Recherche Scientifique (CNRS) and the Netherlands Organization for Scientific Research, for the construction and operation of the Virgo detector and the creation and support of the EGO consortium. The authors also gratefully acknowledge research support from these agencies as well as by the Spanish Agencia Estatal de Investigación, the Conselleria d’Innovació, Universitats, Ciència i Societat Digital de la Generalitat Valenciana and the CERCA Programme Generalitat de Catalunya, Spain, the National Science Centre of Poland and the Foundation for Polish Science (FNP), the European Commission, the Hungarian Scientific Research Fund (OTKA), the French Lyon Institute of Origins (LIO), the Belgian Fonds de la Recherche Scientifique (FRS-FNRS), Actions de Recherche Concertées (ARC) and Fonds Wetenschappelijk Onderzoek – Vlaanderen (FWO), Belgium. The authors gratefully acknowledge the support of the NSF, STFC, INFN, CNRS and Nikhef for provision of computational resources.

Conflicts of Interest: The authors declare no conflict of interest.

Notes

- ¹ A figure of merit to describe the sensitivity of a GW detector to a NS-NS source population. It is defined as the radius R of a Euclidean sphere with the volume equal to the space-time volume surveyed per unit detector time [146].
- ² <https://gracedb.ligo.org/superevents/public/O3/> (accessed on 10 August 2021).
- ³ The T_{90} is an estimate of the duration of the GRB prompt emission. Specifically: T_{90} measures the duration of the time interval during which 90% of the total observed counts have been detected; the start of the T_{90} interval is defined by the time at which 5% of the total counts have been detected, and the end of the T_{90} interval is defined by the time at which 95% of the total counts have been detected.
- ⁴ <https://snews.bnl.gov/> (accessed on 10 August 2021).
- ⁵ A third catalog release is currently in preparation.
- ⁶ The spin-down limit is the maximum GW amplitude the star can reach if only the gravitational wave emission mechanism is considered in the energy budget of the rotating star.

References

1. Maggiore, M. *Gravitational Waves: Volume 2: Astrophysics and Cosmology*, 1st ed.; Oxford University Press: Oxford, UK, 2018; p. 820. [CrossRef]
2. The LIGO Scientific Collaboration Advanced LIGO. *Class. Quantum Gravity* **2015**, *32*, 074001. [CrossRef]
3. Acernese, F.; Agathos, M.; Agatsuma, K.; Aisa, D.; Allemandou, N.; Allocca, A.; Amarni, J.; Astone, P.; Balestri, G.; Ballardín, G.; et al. Advanced Virgo: A second-generation interferometric gravitational wave detector. *Class. Quant. Grav.* **2015**, *32*, 024001.
4. The LIGO Scientific Collaboration; The Virgo Collaboration GWTC-1: A Gravitational-Wave Transient Catalog of Compact Binary Mergers Observed by LIGO and Virgo during the First and Second Observing Runs. *Phys. Rev. X* **2019**, *9*, 031040.
5. Abbott, R.; Abbott, T. D.; Abraham, S.; Acernese, F.; Ackley, K.; Adams, A.; Adams, C.; Adhikari, R. X.; Adya, V. B.; Affeldt, C.; et al. GWTC-2: Compact Binary Coalescences Observed by LIGO and Virgo During the First Half of the Third Observing Run. *arXiv* **2020**, arXiv:2010.14527.

6. The LIGO Scientific Collaboration; The Virgo Collaboration; The LIGO Scientific Collaboration; The Virgo Collaboration Properties of the Binary Black Hole Merger GW150914. *Phys. Rev. D* **2016**, *116*, 241102.
7. Metzger, B.D.; Berger, E. What is the Most Promising Electromagnetic Counterpart of a Neutron Star Binary Merger? *Astrophys. J.* **2012**, *746*, 48.
8. Perna, R.; Lazzati, D.; Giacomazzo, B. Short Gamma-Ray Bursts from the Merger of Two Black Holes. *Astrophys. J. Lett.* **2016**, *821*, L18.
9. Bartos, I.; Haiman, Z.; Marka, Z.; Metzger, B.D.; Stone, N.C.; Marka, S. Gravitational-wave localization alone can probe origin of stellar-mass black hole mergers. *Nat. Commun.* **2017**, *8*, 831.
10. Graham, M.J.; Ford, K.E.S.; McKernan, B.; Ross, N.P.; Stern, D.; Burdge, K.; Coughlin, M.; Djorgovski, S.G.; Drake, A.J.; Duev, D.; et al. Candidate Electromagnetic Counterpart to the Binary Black Hole Merger Gravitational-Wave Event S190521g*. *Phys. Rev. D* **2020**, *124*, 251102.
11. Kotake, K.; Sato, K.; Takahashi, K. Explosion mechanism, neutrino burst and gravitational wave in core-collapse supernovae. *Rep. Prog. Phys.* **2006**, *69*, 971–1143.
12. Ott, C.D. Topical Review: The gravitational-wave signature of core-collapse supernovae. *Class. Quantum Gravity* **2009**, *26*, 063001.
13. Gossan, S.E.; Sutton, P.; Stuver, A.; Zanolin, M.; Gill, K.; Ott, C.D. Observing gravitational waves from core-collapse supernovae in the advanced detector era. *Phys. Rev. D* **2016**, *93*, 042002.
14. The LIGO Scientific Collaboration; The Virgo Collaboration. Optically targeted search for gravitational waves emitted by core-collapse supernovae during the first and second observing runs of advanced LIGO and advanced Virgo. *Phys. Rev. D* **2020**, *101*, 084002.
15. Soderberg, A.M.; Berger, E.; Page, K.L.; Schady, P.; Parrent, J.; Pooley, D.; Wang, X.Y.; Ofek, E.O.; Cucchiara, A.; Rau, A.; et al. An extremely luminous X-ray outburst at the birth of a supernova. *Nature* **2008**, *453*, 469–474.
16. Garnavich, P.M.; Tucker, B.E.; Rest, A.; Shaya, E.J.; Olling, R.P.; Kasen, D.; Villar, A. Shock Breakout and Early Light Curves of Type II-P Supernovae Observed with Kepler. *Astrophys. J.* **2016**, *820*, 23.
17. Hjorth, J.; Sollerman, J.; Møller, P.; Fynbo, J.P.U.; Woosley, S.E.; Kouveliotou, C.; Tanvir, N.R.; Greiner, J.; Andersen, M.I.; Castro-Tirado, A.J.; et al. A very energetic supernova associated with the γ -ray burst of 29 March 2003. *Nature* **2003**, *423*, 847–850.
18. Stanek, K.Z.; Matheson, T.; Garnavich, P.M.; Martini, P.; Berlind, P.; Caldwell, N.; Challis, P.; Brown, W.R.; Schild, R.; Krisciunas, K.; et al. Spectroscopic Discovery of the Supernova 2003dh Associated with GRB 030329. *Astrophys. J. Lett.* **2003**, *591*, L17–L20.
19. Hirata, K.; Kajita, T.; Koshihara, M.; Nakahata, M.; Oyama, Y.; Sato, N.; Suzuki, A.; Takita, M.; Totsuka, Y.; Kifune, T.; et al. Observation of a neutrino burst from the supernova SN1987A. *Phys. Rev. D* **1987**, *58*, 1490–1493. [[CrossRef](#)] [[PubMed](#)]
20. Bionta, R.M.; Blewitt, G.; Bratton, C.B.; Casper, D.; Ciocio, A.; Claus, R.; Cortez, B.; Crouch, M.; Dye, S.T.; Errede, S.; et al. Observation of a neutrino burst in coincidence with supernova 1987A in the Large Magellanic Cloud. *Phys. Rev. D* **1987**, *58*, 1494–1496. [[CrossRef](#)]
21. Alexeyev, E.N.; Alexeyeva, L.N.; Krivosheina, I.V.; Volchenko, V.I. Detection of the neutrino signal from SN 1987A in the LMC using the INR Baksan underground scintillation telescope. *Phys. Lett. B* **1988**, *205*, 209–214. [[CrossRef](#)]
22. Murase, K. New prospects for detecting high-energy neutrinos from nearby supernovae. *Phys. Rev. D* **2018**, *97*, 081301.
23. Lasky, P.D. Gravitational Waves from Neutron Stars: A Review. *Publ. Astron. Soc. Aust.* **2015**, *32*, e034.
24. Beloborodov, A.M.; Thompson, C. Corona of Magnetars. *Astrophys. J.* **2007**, *657*, 967–993.
25. Corsi, A.; Owen, B.J. Maximum gravitational-wave energy emissible in magnetar flares. *Phys. Rev. D* **2011**, *83*, 104014.
26. Mereghetti, S. The strongest cosmic magnets: Soft gamma-ray repeaters and anomalous X-ray pulsars. *Astron. Astrophys. Rev.* **2008**, *15*, 225–287.
27. Espinoza, C.M.; Lyne, A.G.; Stappers, B.W.; Kramer, M. A study of 315 glitches in the rotation of 102 pulsars. *Mon. Not. R. Astron. Soc.* **2011**, *414*, 1679–1704.
28. Haskell, B.; Schwenzer, K. Gravitational waves from isolated neutron stars. *arXiv* **2021**, arXiv:2104.03137.
29. Glampedakis, K.; Gualtieri, L., Gravitational Waves from Single Neutron Stars: An Advanced Detector Era Survey. In *The Physics and Astrophysics of Neutron Stars*; Rezzolla, L., Pizzochero, P., Jones, D.I., Rea, N., Vidaña, I., Eds.; Springer International Publishing: Cham, Switzerland, 2018; pp. 673–736. [[CrossRef](#)]
30. Aasi, J.; Abadie, J.; Abbott, B. P.; Abbott, R.; Abbott, T.; Abernathy, M. R.; Accadia, T.; Acernese, F.; Adams, C.; Adams, T.; et al. Gravitational Waves from Known Pulsars: Results from the Initial Detector Era. *Astrophys. J.* **2014**, *785*, 119.
31. The LIGO Scientific Collaboration; The Virgo Collaboration; The KAGRA Collaboration. Constraints from LIGO O3 data on gravitational-wave emission due to r-modes in the glitching pulsar PSR J0537-6910. *arXiv* **2021**, arXiv:2104.14417.
32. Abbott, R.; Abbott, T. D.; Abraham, S.; Acernese, F.; Ackley, K.; Adams, A.; Adams, C.; Adhikari, R. X.; Adya, V. B.; Affeldt, C.; et al. Gravitational-wave Constraints on the Equatorial Ellipticity of Millisecond Pulsars. *Astrophys. J. Lett.* **2020**, *902*, L21. [[CrossRef](#)]
33. The LIGO Scientific Collaboration; The Virgo Collaboration; The KAGRA Collaboration. Diving below the Spin-down Limit: Constraints on Gravitational Waves from the Energetic Young Pulsar PSR J0537-6910. *Astrophys. J. Lett.* **2021**, *913*, L27. [[CrossRef](#)]
34. Abbott, R.; Abbott, T.D.; Abraham, S.; Acernese, F.; Ackley, K.; Adams, A.; Adams, C.; Adhikari, R.X.; Adya, V.B.; Affeldt, C.; et al. Searches for continuous gravitational waves from young supernova remnants in the early third observing run of Advanced LIGO and Virgo. *arXiv* **2021**, arXiv:2105.11641.

35. Lindblom, L.; Owen, B.J. Directed searches for continuous gravitational waves from twelve supernova remnants in data from Advanced LIGO's second observing run. *Phys. Rev. D* **2020**, *101*. [[CrossRef](#)]
36. Papa, M.A.; Ming, J.; Gotthelf, E.V.; Allen, B.; Prix, R.; Dergachev, V.; Eggenstein, H.B.; Singh, A.; Zhu, S.J. Search for Continuous Gravitational Waves from the Central Compact Objects in Supernova Remnants Cassiopeia A, Vela Jr., and G347.3–0.5. *Astrophys. J.* **2020**, *897*, 22. [[CrossRef](#)]
37. Piccinni, O.J.; Astone, P.; D'Antonio, S.; Frasca, S.; Intini, G.; La Rosa, I.; Leaci, P.; Mastrogiovanni, S.; Miller, A.; Palomba, C. Directed search for continuous gravitational-wave signals from the Galactic Center in the Advanced LIGO second observing run. *Phys. Rev. D* **2020**, *101*. [[CrossRef](#)]
38. The LIGO Scientific Collaboration; The Virgo Collaboration All-sky search for continuous gravitational waves from isolated neutron stars using Advanced LIGO O2 data. *Phys. Rev. D* **2019**, *100*. [[CrossRef](#)]
39. The LIGO Scientific Collaboration; The Virgo Collaboration All-sky search in early O3 LIGO data for continuous gravitational-wave signals from unknown neutron stars in binary systems. *Phys. Rev. D* **2021**, *103*, 064017. [[CrossRef](#)]
40. Riles, K. Recent searches for continuous gravitational waves. *Mod. Phys. Lett. A* **2017**, *32*, 1730035. [[CrossRef](#)]
41. Sieniawska, M.; Beijger, M. Continuous Gravitational Waves from Neutron Stars: Current Status and Prospects. *Universe* **2019**, *5*, 217.
42. Lattimer, J.M.; Prakash, M. The Physics of Neutron Stars. *Science* **2004**, *304*, 536–542. [[CrossRef](#)]
43. Buonanno, A.; Sigl, G.; Raffelt, G.G.; Janka, H.T.; Müller, E. Stochastic gravitational-wave background from cosmological supernovae. *Phys. Rev. D* **2005**, *72*, 084001.
44. Howell, E.; Coward, D.; Burman, R.; Blair, D.; Gilmore, J. The gravitational wave background from neutron star birth throughout the cosmos. *Mon. Not. R. Astron. Soc.* **2004**, *351*, 1237–1246. [[CrossRef](#)]
45. Sandick, P.; Olive, K.A.; Daigne, F.; Vangioni, E. Gravitational waves from the first stars. *Phys. Rev. D* **2006**, *73*, 104024.
46. Caldwell, R.R.; Allen, B. Cosmological constraints on cosmic-string gravitational radiation. *Phys. Rev. D* **1992**, *45*, 3447–3468. [[CrossRef](#)] [[PubMed](#)]
47. Damour, T.; Vilenkin, A. Gravitational radiation from cosmic (super)strings: Bursts, stochastic background, and observational windows. *Phys. Rev. D* **2005**, *71*, 063510.
48. Ölmez, S.; Mandic, V.; Siemens, X. Gravitational-wave stochastic background from kinks and cusps on cosmic strings. *Phys. Rev. D* **2010**, *81*, 104028.
49. Grishchuk, L.P. Relic gravitational waves and limits on inflation. *Phys. Rev. D* **1993**, *48*, 3513–3516.
50. Easther, R.; Giblin, John T., J.; Lim, E.A. Gravitational Wave Production at the End of Inflation. *Phys. Rev. D* **2007**, *99*, 221301.
51. Cook, J.L.; Sorbo, L. Particle production during inflation and gravitational waves detectable by ground-based interferometers. *Phys. Rev. D* **2012**, *85*, 023534.
52. The LIGO Scientific Collaboration; The Virgo Collaboration GW170817: Implications for the Stochastic Gravitational-Wave Background from Compact Binary Coalescences. *Phys. Rev. D* **2018**, *120*, 091101.
53. Bertone, G.; Hooper, D. History of dark matter. *Rev. Mod. Phys.* **2018**, *90*, 045002.
54. Bertone, G.; Croon, D.; Amin, M.; Boddy, K.K.; Kavanagh, B.; Mack, K.J.; Natarajan, P.; Opferkuch, T.; Schutz, K.; Takhistov, V.; et al. Gravitational wave probes of dark matter: Challenges and opportunities. *SciPost Phys. Core* **2020**, *3*. [[CrossRef](#)]
55. Arvanitaki, A.; Dimopoulos, S.; Dubovsky, S.; Kaloper, N.; March-Russell, J. String axiverse. *Phys. Rev. D* **2010**, *81*, 123530. [[CrossRef](#)]
56. Brito, R.; Cardoso, V.; Pani, P. Superradiance. *Lect. Notes Phys.* **2020**. [[CrossRef](#)]
57. Peccei, R.D.; Quinn, H.R. CP Conservation in the Presence of Instantons. *Phys. Rev. Lett.* **1977**, *38*, 1440–1443. [[CrossRef](#)]
58. Clesse, S.; García-Bellido, J. Massive primordial black holes from hybrid inflation as dark matter and the seeds of galaxies. *Phys. Rev. D* **2015**, *92*, 023524. [[CrossRef](#)]
59. Chapline, G.F. Cosmological effects of primordial black holes. *Nature* **1975**, *253*, 251–252. [[CrossRef](#)]
60. Weber, J. Gravitational-Wave-Detector Events. *Phys. Rev. Lett.* **1968**, *20*, 1307–1308. [[CrossRef](#)]
61. La Rana, A.; Milano, L. The Early History of Gravitational Wave Detection in Italy: From the First Resonant Bars to the Beginning of the Virgo Collaboration. 2017. Available online: <https://www.paviauniversitypress.it/articolo/9788869520709-c17/539> (accessed on 10 August 2021).
62. ROG Collaboration Explorer Experiment Home Page. Available online: http://www.lnf.infn.it/esperimenti/rog/frame_explorer.htm (accessed on 19 June 2021).
63. Astone, P.; Bassan, M.; Bonifazi, P.; Carelli, P.; Castellano, M.G.; Cavallari, G.; Coccia, E.; Cosmelli, C.; Fafone, V.; Frasca, S.; et al. Long-term operation of the Rome “Explorer” cryogenic gravitational wave detector. *Phys. Rev. D* **1993**, *47*, 362–375. [[CrossRef](#)]
64. ROG Collaboration Nautilus Experiment Home Page. Available online: http://www.lnf.infn.it/esperimenti/rog/frame_nautilus.htm (accessed on 19 June 2021).
65. Astone, P.; Bassan, M.; Bonifazi, P.; Carelli, P.; Coccia, E.; Cosmelli, C.; Fafone, V.; Frasca, S.; Marini, A.; Mazzitelli, G.; et al. The gravitational wave detector NAUTILUS operating at T = 0.1 K. *Astropart. Phys.* **1997**, *7*, 231–243. [[CrossRef](#)]
66. AURIGA Collaboration AURIGA Experiment Home Page. Available online: <http://www.auriga.lnf.infn.it/> (accessed on 19 June 2021).

67. Zendri, J.P.; Baggio, L.; Bignotto, M.; Bonaldi, M.; Cerdonio, M.; Conti, L.; Rosa, M.D.; Falferi, P.; Fortini, P.L.; Inguscio, M.; et al. Status report and near future prospects for the gravitational wave detector AURIGA. *Class. Quantum Gravity* **2002**, *19*, 1925–1933. [[CrossRef](#)]
68. Mauceli, E.; Geng, Z.K.; Hamilton, W.O.; Johnson, W.W.; Merkwowitz, S.; Morse, A.; Price, B.; Solomonson, N. The Allegro gravitational wave detector: Data acquisition and analysis. *Phys. Rev. D* **1996**, *54*, 1264–1275. [[CrossRef](#)]
69. Blair, D.G.; Ivanov, E.N.; Tobar, M.E.; Turner, P.J.; van Kann, F.; Heng, I.S. High Sensitivity Gravitational Wave Antenna with Parametric Transducer Readout. *Phys. Rev. Lett.* **1995**, *74*, 1908–1911. [[CrossRef](#)] [[PubMed](#)]
70. IGEC Collaboration The International Gravitational Event Collaboration Home Page. Available online: <http://igec.lnl.infn.it/> (accessed on 19 June 2021).
71. Astone, P.; Babusci, D.; Baggio, L.; Bassan, M.; Blair, D.G.; Bonaldi, M.; Bonifazi, P.; Busby, D.; Carelli, P.; Cerdonio, M.; et al. Methods and results of the IGEC search for burst gravitational waves in the years 1997–2000. *Phys. Rev. D* **2003**, *68*, 022001. [[CrossRef](#)]
72. Astone, P.; Babusci, D.; Baggio, L.; Bassan, M.; Bignotto, M.; Bonaldi, M.; Camarda, M.; Carelli, P.; Cavallari, G.; Cerdonio, M.; et al. Results of the IGEC-2 search for gravitational wave bursts during 2005. *Phys. Rev. D* **2007**, *76*, 102001. [[CrossRef](#)]
73. INFN. INFN Home Page. Frascati (RM). 2021. Available online: <https://home.infn.it/en/> (accessed on 10 August 2021).
74. Parigi Collaboration (Pisa, Napoli, Frascati, Orsay). Antenna Interferometrica a Grande Base per la Ricerca di Onde Gravitazionali. Technical Report VIR-0473B-15; INFN PI/AE 87/1; 1987. Available online: <https://tds.virgo-gw.eu/ql/?c=11203> (accessed on 25 August 2021).
75. CNRS. CNRS Home Page. Available online: <http://www.cnrs.fr/en> (accessed on 19 June 2021).
76. Giazotto, A.; Campani, E.; Passuello, D.; Stefanini, A. Performance of an Active Pendulum with Interferometric Sensing 1986. In Proceedings of the Fourth Marcel Grossmann Meeting, Rome, Italy, 17–21 June 1985.
77. Del Fabbro, R.; Di Virgilio, A.; Giazotto, A.; Kautzky, H.; Montelatici, V.; Passuello, D. Three-dimensional seismic super-attenuator for low frequency gravitational wave detection. *Phys. Lett. A* **1987**, *124*, 253–257. [[CrossRef](#)]
78. Caron, B.; Dominjon, A.; Drezen, C.; Flaminio, R.; Grave, X.; Marion, F.; Massonnet, L.; Mehmél, C.; Morand, R.; Mours, B.; et al. Status of the VIRGO experiment. *Nucl. Phys. B Proc. Suppl.* **1996**, *48*, 107–109. [[CrossRef](#)]
79. EGO. Virgo R&D and Interdisciplinarity. Available online: <https://www.ego-gw.it/rd-interdisciplinarity/> (accessed on 13 June 2021).
80. The Virgo Collaboration; The LIGO Scientific Collaboration. MOU between VIRGO and LIGO. Available online: <https://tds.virgo-gw.eu/ql/?c=1632> (accessed on 1 July 2021).
81. Accadia, T.; Acernese, F.; Alshourbagy, M.; Amico, P.; Antonucci, F.; Aoudia, S.; Giordano, G. Virgo: A laser interferometer to detect gravitational waves. *J. Instrum.* **2012**, *7*, P03012. [[CrossRef](#)]
82. The Virgo Collaboration. *Advanced Virgo Technical Design Report*; Technical Report VIR-0128A-12; 2012. Available online: <https://tds.virgo-gw.eu/ql/?c=8940> (accessed on 1 July 2021).
83. The LIGO Scientific Collaboration; The Virgo Collaboration Observation of Gravitational Waves from a Binary Black Hole Merger. *Phys. Rev. Lett.* **2016**, *116*, 061102.
84. The LIGO Scientific Collaboration; The Virgo Collaboration GW170814: A Three-Detector Observation of Gravitational Waves from a Binary Black Hole Coalescence. *Phys. Rev. Lett.* **2017**, *119*, 141101. [[CrossRef](#)]
85. The LIGO Scientific Collaboration; The Virgo Collaboration GW170817: Observation of Gravitational Waves from a Binary Neutron Star Inspiral. *Phys. Rev. D* **2017**, *119*, 161101.
86. Aso, Y.; Michimura, Y.; Somiya, K.; Ando, M.; Miyakawa, O.; Sekiguchi, T.; Tatsumi, D.; Yamamoto, H. Interferometer design of the KAGRA gravitational wave detector. *Phys. Rev. D* **2013**, *88*, 043007. [[CrossRef](#)]
87. Nikhef. Nikhef Home Page. Available online: <https://www.nikhef.nl/en/> (accessed on 21 June 2021).
88. Hild, S.; Grote, H.; Degallaix, J.; Chelkowski, S.; Danzmann, K.; Freise, A.; Hewitson, M.; Hough, J.; Lück, H.; Prijatelj, M.; et al. DC-readout of a signal-recycled gravitational wave detector. *Class. Quantum Gravity* **2009**, *26*, 055012. [[CrossRef](#)]
89. Acernese, F.; Alshourbagy, M.; Antonucci, F.; Aoudia, S.; Arun, K.G.; Astone, P.; Ballardín, G.; Barone, F.; Barsuglia, M.; Bauer, T.S.; et al. Automatic Alignment for the first science run of the Virgo interferometer. *Astropart. Phys.* **2010**, *33*, 131–139. [[CrossRef](#)]
90. Acernese, F.; Adams, T.; Agatsuma, K.; Aiello, L.; Allocca, A.; Amato, A.; Antier, S.; Arnaud, N.; Ascenzi, S.; Astone, P.; et al. Status of Advanced Virgo. *EPJ Web Conf.* **2018**, *182*, 02003. [[CrossRef](#)]
91. Beker, M.G.; van den Brand, J.F.J.; Hennes, E.; Rabeling, D.S. Newtonian noise and ambient ground motion for gravitational wave detectors. *J. Phys. Conf. Ser.* **2012**, *363*, 012004. [[CrossRef](#)]
92. Harms, J. Terrestrial Gravity Fluctuations. *Living Rev. Relativ.* **2015**, *18*. [[CrossRef](#)] [[PubMed](#)]
93. Harms, J.; Venkateswara, K. Newtonian-noise cancellation in large-scale interferometric GW detectors using seismic tiltmeters. *Class. Quantum Gravity* **2016**, *33*, 234001. [[CrossRef](#)]
94. Tringali, M.C.; Bulik, T.; Harms, J.; Fiori, I.; Paoletti, F.; Singh, N.; Idzkowski, B.; Kutynia, A.; Nikliborc, K.; Suchiński, M.; et al. Seismic array measurements at Virgo’s west end building for the configuration of a Newtonian-noise cancellation system. *Class. Quantum Gravity* **2019**, *37*, 025005. [[CrossRef](#)]
95. Singha, A.; Hild, S.; Harms, J. Newtonian-noise reassessment for the Virgo gravitational-wave observatory including local recess structures. *Class. Quantum Gravity* **2020**, *37*. [[CrossRef](#)]

96. Badaracco, F.; Harms, J. Optimization of seismometer arrays for the cancellation of Newtonian noise from seismic body waves. *Class. Quantum Gravity* **2019**, *36*, 145006. [[CrossRef](#)]
97. Ballardín, G.; Bracci, L.; Braccini, S.; Bradaschia, C.; Casciano, C.; Calamai, G.; Cavalieri, R.; Cecchi, R.; Cella, G.; Cuoco, E.; et al. Measurement of the VIRGO superattenuator performance for seismic noise suppression. *Rev. Sci. Instruments* **2001**, *72*. [[CrossRef](#)]
98. Aisa, D.; Aisa, S.; Campeggi, C.; Colombini, M.; Conte, A.; Farnesini, L.; Vocca, H. The Advanced Virgo monolithic fused silica suspension. *Nucl. Instruments Methods Phys. Res. Sect. A Accel. Spectrometers Detect. Assoc. Equip.* **2016**, *824*, 644–645.
99. Naticchioni, L. The payloads of Advanced Virgo: Current status and upgrades. *J. Phys. Conf. Ser.* **2018**, *957*, 012002. [[CrossRef](#)]
100. Acernese, F.; Antonucci, F.; Aoudia, S.; Arun, K.G.; Astone, P.; Ballardín, G.; Barone, F.; Barsuglia, M.; Bauer, T.S.; Beker, M.G.; et al. Measurements of Superattenuator seismic isolation by Virgo interferometer. *Astropart. Phys.* **2010**, *33*, 182–189. [[CrossRef](#)]
101. Callen, H.B.; Welton, T.A. Irreversibility and Generalized Noise. *Phys. Rev.* **1951**, *83*, 34–40. [[CrossRef](#)]
102. Penn, S.D.; Harry, G.M.; Gretarsson, A.M.; Kittelberger, S.E.; Saulson, P.R.; Schiller, J.J.; Smith, J.R.; Swords, S.O. High quality factor measured in fused silica. *Rev. Sci. Instrum.* **2001**, *72*, 3670–3673.
103. Gretarsson, A.M.; Harry, G.M. Dissipation of mechanical energy in fused silica fibers. *Rev. Sci. Instrum.* **1999**, *70*, 4081–4087.
104. Heptonstall, A.; Barton, M.A.; Bell, A.S.; Bohn, A.; Cagnoli, G.; Cumming, A.; Grant, A.; Gustafson, E.; Hammond, G.D.; Hough, J.; et al. Enhanced characteristics of fused silica fibers using laser polishing. *Class. Quantum Gravity* **2014**, *31*, 105006. [[CrossRef](#)]
105. Rowan, S.; Twyford, S.; Hutchins, R.; Kovalik, J.; Logan, J.; McLaren, A.; Robertson, N.; Hough, J. Q factor measurements on prototype fused quartz pendulum suspensions for use in gravitational wave detectors. *Phys. Lett. A* **1997**, *233*, 303–308. [[CrossRef](#)]
106. Gianpietro, C.; Gammaitoni, L.; Hough, J.; Kovalik, J.; McIntosh, S.; Punturo, M.; Rowan, S. Very High Q Measurements on a Fused Silica Monolithic Pendulum for Use in Enhanced Gravity Wave Detectors. *Phys. Rev. Lett.* **2000**, *85*, 2442–2445. [[CrossRef](#)]
107. Amico, P.; Bosi, L.; Carbone, L.; Gammaitoni, L.; Punturo, M.; Travasso, F.; Vocca, H. Fused silica suspension for the VIRGO optics: Status and perspectives. *Class. Quant. Grav.* **2002**, *19*, 1669–1674. [[CrossRef](#)]
108. Plissi, M.; Torrie, C.; Husman, M.; Robertson, N.; Strain, K.; Ward, H.; Lück, H.; Hough, J. GEO 600 triple pendulum suspension system: Seismic isolation and control. *Rev. Sci. Instruments* **2000**, *71*, 2539–2545. [[CrossRef](#)]
109. Smith, J.; Gianpietro, C.; Crooks, D.; Fejer, M.; Gossler, S.; Lück, H.; Rowan, S.; Hough, J.; Danzmann, K. Mechanical quality factor measurements of monolithically-suspended fused silica test masses of the GEO600 gravitational wave detector. *Class. Quantum Gravity* **2004**, *21*. [[CrossRef](#)]
110. Lorenzini, M. The monolithic suspension for the Virgo interferometer. *Class. Quant. Grav.* **2010**, *27*, 084021. [[CrossRef](#)]
111. Cumming, A.V.; Bell, A.S.; Barsotti, L.; Barton, M.A.; Cagnoli, G.; Cook, D.; Cunningham, L.; Evans, M.; Hammond, G.D.; Harry, G.M.; et al. Design and development of the advanced LIGO monolithic fused silica suspension. *Class. Quantum Gravity* **2012**, *29*, 035003. [[CrossRef](#)]
112. Heptonstall, A.; Barton, M.; Bell, A.; Cagnoli, G.; Cantley, C.; Crooks, D.; Cumming, A.; Grant, A.; Hammond, G.; Harry, G.; et al. Invited article: CO₂ laser production of fused silica fibers for use in interferometric gravitational wave detector mirror suspensions. *Rev. Sci. Instruments* **2011**, *82*, 011301. [[CrossRef](#)]
113. Montani, M.; on behalf of the Virgo Collaboration. Silica Fibers Production and Characterization for Future Gravitational Waves Detectors. Proceedings of the GRAVitational-wave Science&technology Symposium 2019 (GRASS2019), Padova, Italy, 17–18 October 2019. [[CrossRef](#)]
114. Piergiovanni, F.; Lorenzini, M.; Cagnoli, G.; Campagna, E.; Cesarini, E.; Losurdo, G.; Martelli, F.; Vetrano, F.; Viceré, A. The dynamics of monolithic suspensions for advanced detectors: A 3-segment model. *J. Phys. Conf. Ser.* **2010**, *228*, 012017. [[CrossRef](#)]
115. Cagnoli, G.; Willems, P.A. Effects of nonlinear thermoelastic damping in highly stressed fibers. *Phys. Rev. B* **2002**, *65*, 174111. [[CrossRef](#)]
116. Cagnoli, G.; Gammaitoni, L.; Kovalik, J.; Marchesoni, F.; Punturo, M. Full scale prototype of high Q pendulum for interferometric gravitational wave detectors. *Rev. Sci. Instrum.* **2000**, *71*, 2206–2210. [[CrossRef](#)]
117. Dari, A.; Travasso, F.; Vocca, H.; Gammaitoni, L. Breaking strength tests on silicon and sapphire bondings for gravitational wave detectors. *Class. Quantum Gravity* **2010**, *27*, 045010. [[CrossRef](#)]
118. Cimma, B.; Forest, D.; Ganau, P.; Lagrange, B.; Mackowski, J.M.; Michel, C.; Montorio, J.L.; Morgado, N.; Pignard, R.; Pinard, L.; et al. Ion beam sputtering coatings on large substrates: Toward an improvement of the mechanical and optical performances. *Appl. Opt.* **2006**, *45*, 1436–1439. [[CrossRef](#)]
119. Pinard, L.; Michel, C.; Sassolas, B.; Balzarini, L.; Degallaix, J.; Dolique, V.; Flaminio, R.; Forest, D.; Granata, M.; Lagrange, B.; et al. Mirrors used in the LIGO interferometers for first detection of gravitational waves. *Appl. Opt.* **2017**, *56*, C11–C15. [[CrossRef](#)]
120. Numata, K.; Yamamoto, K.; Ishimoto, H.; Otsuka, S.; Kawabe, K.; Ando, M.; Tsubono, K. Systematic measurement of the intrinsic losses in various kinds of bulk fused silica. *Phys. Lett. A* **2004**, *327*, 263–271. [[CrossRef](#)]
121. Crooks, D.R.M.; Sneddon, P.; Cagnoli, G.; Hough, J.; Rowan, S.; Fejer, M.M.; Gustafson, E.; Route, R.; Nakagawa, N.; Coyne, D.; et al. Excess mechanical loss associated with dielectric mirror coatings on test masses in interferometric gravitational wave detectors. *Class. Quantum Gravity* **2002**, *19*, 4229. [[CrossRef](#)]
122. Granata, M.; Amato, A.; Cagnoli, G.; Coulon, M.; Degallaix, J.; Forest, D.; Mereni, L.; Michel, C.; Pinard, L.; Sassolas, B.; et al. Progress in the measurement and reduction of thermal noise in optical coatings for gravitational-wave detectors. *Appl. Opt.* **2020**, *59*, A229–A235. [[CrossRef](#)] [[PubMed](#)]

123. Amato, A.; Cagnoli, G.; Canepa, M.; Coillet, E.; Degallaix, J.; Dolique, V.; Forest, D.; Granata, M.; Martinez, V.; Michel, C.; et al. High-Reflection Coatings for Gravitational-Wave Detectors: State of The Art and Future Developments. *J. Phys. Conf. Ser.* **2018**, *957*, 012006. [[CrossRef](#)]
124. Gras, S.; Evans, M. Direct measurement of coating thermal noise in optical resonators. *Phys. Rev. D* **2018**, *98*, 122001. [[CrossRef](#)]
125. Granata, M.; Amato, A.; Balzarini, L.; Canepa, M.; Degallaix, J.; Forest, D.; Dolique, V.; Mereni, L.; Michel, C.; Pinard, L.; et al. Amorphous optical coatings of present gravitational-wave interferometers. *Class. Quantum Gravity* **2020**, *37*, 095004. [[CrossRef](#)]
126. Agresti, J.; Castaldi, G.; Desalvo, R.; Galdi, V.; Pierro, V.; Pinto, I. Optimized multilayer dielectric mirror coatings for gravitational wave interferometers. *Proc. SPIE* **2006**, *6286*, 628608. [[CrossRef](#)]
127. Piergiovanni, F.; on behalf of the Virgo Collaboration. The research on amorphous coatings for future GW detectors. *J. Phys. Conf. Ser.* **2020**, *1468*, 012216. [[CrossRef](#)]
128. Max Planck Institute for Gravitational Physics (Albert Einstein Institute) AEI Homepage. Available online: <https://www.aei.mpg.de/> (accessed on 1 July 2021).
129. Drever, R.W.P.; Hall, J.L.; Kowalski, F.V.; Hough, J.; Ford, G.M.; Munley, A.J.; Ward, H. Laser phase and frequency stabilization using an optical resonator. *Appl. Phys. B* **1983**, *31*, 97–105. [[CrossRef](#)]
130. Black, E.D. An introduction to Pound–Drever–Hall laser frequency stabilization. *Am. J. Phys.* **2001**, *69*, 79. [[CrossRef](#)]
131. Vahlbruch, H.; Chelkowski, S.; Hage, B.; Franzen, A.; Danzmann, K.; Schnabel, R. Coherent control of vacuum squeezing in the gravitational-wave detection band. *Phys. Rev. Lett.* **2006**, *97*, 011101. [[CrossRef](#)] [[PubMed](#)]
132. Mehmet, M.; Vahlbruch, H. High-efficiency squeezed light generation for gravitational wave detectors. *Class. Quantum Gravity* **2018**, *36*, 015014. [[CrossRef](#)]
133. Mehmet, M.; Vahlbruch, H. The Squeezed Light Source for the Advanced Virgo Detector in the Observation Run O3. *Galaxies* **2020**, *8*, 79. [[CrossRef](#)]
134. Acernese, F.; Agathos, M.; Aiello, L.; Allocca, A.; Amato, A.; Ansoldi, S.; Antier, S.; Arène, M.; Arnaud, N.; Ascenzi, S.; et al. Increasing the astrophysical reach of the advanced Virgo detector via the application of squeezed vacuum states of light. *Phys. Rev. Lett.* **2019**, *123*, 231108. [[CrossRef](#)]
135. Mantovani, M.; Vajente, G. *Alignment Accuracy Requirements for Advanced Virgo*; Technical Report VIR-0247A-10; 2010. Available online: <https://tds.virgo-gw.eu/ql/?c=7384> (accessed on 10 August 2021).
136. Mantovani, M. *Automatic Alignment Sensing and Control Scheme for Advanced Virgo MSRC Configuration*; Technical Report VIR-0201A-11; 2011. Available online: <https://tds.virgo-gw.eu/ql/?c=8255> (accessed on 10 August 2021).
137. Bersanetti, D.; Casanueva Diaz, J.; Allocca, A.; Heitmann, H.; Hoak, D.; Mantovani, M.; Ruggi, P.; Swinkels, B. New algorithm for the Guided Lock technique for a high-Finesse optical cavity. *Astropart. Phys.* **2020**, *117*, 102405. [[CrossRef](#)]
138. Acernese, F.; Agathos, M.; Aiello, L.; Allocca, A.; Aloy, M.A.; Amato, A.; Antier, S.; Arène, M.; Arnaud, N.; Ascenzi, S.; et al. The advanced Virgo longitudinal control system for the O2 observing run. *Astropart. Phys.* **2020**, *116*, 102386. [[CrossRef](#)]
139. Allocca, A.; Bersanetti, D.; Casanueva Diaz, J.; De Rossi, C.; Mantovani, M.; Masserot, A.; Rolland, L.; Ruggi, P.; Swinkels, B.; Tapia San Martin, E.N.; et al. Interferometer Sensing and Control for the Advanced Virgo Experiment in the O3 Scientific Run. *Galaxies* **2020**, *8*, 85. [[CrossRef](#)]
140. Lawrence, R.C. *Active Wavefront Correction in Laser Interferometric Gravitational Wave Detectors*. Ph.D. Thesis, Massachusetts Institute of Technology, Cambridge, MA, USA, 2003.
141. Brooks, A.F. *Hartmann Wavefront Sensors for Advanced Gravitational Wave Interferometers*. Ph.D. Thesis, School of Chemistry and Physics, University of Adelaide, Adelaide, Australia, 2007.
142. Nardecchia, I. *Control of Optical Aberrations in Advanced Interferometric Gravitational Wave Detectors*. Ph.D. Thesis, Università degli Studi di Roma La Sapienza and Università degli Studi di Roma Tor Vergata, Roma, Italy, 2016.
143. Aiello, L.; Cesarini, E.; Fafone, V.; Lorenzini, M.; Minenkov, Y.; Nardecchia, I.; Rocchi, A.; Sequino, V. Thermal compensation system in advanced and third generation gravitational wave interferometric detectors. *J. Phys. Conf. Ser.* **2019**, *1226*, 012019. [[CrossRef](#)]
144. Aiello, L. *Development of New Approaches for Optical Aberration Control in Gravitational Wave Interferometers*. Ph.D. Thesis, Gran Sasso Science Institute, L'Aquila, Italy, 2019.
145. The LIGO Scientific Collaboration; The Virgo Collaboration; The KAGRA Collaboration Prospects for observing and localizing gravitational-wave transients with Advanced LIGO, Advanced Virgo and KAGRA. *Living Rev. Relativ.* **2020**, *23*, 3. [[CrossRef](#)] [[PubMed](#)]
146. LIGO/Virgo Collaborations LIGO/Virgo Public Alerts User Guide. Available online: <https://emfollow.docs.ligo.org/userguide/glossary.html> (accessed on 2 August 2021).
147. Gravitational Wave Open Science Center O3b Summary Page. Available online: https://www.gw-openscience.org/detector_status/O3b/ (accessed on 24 June 2021).
148. LIGO Instrument Science Sensitivity and performance of the Advanced LIGO detectors in the third observing run. *Phys. Rev. D* **2020**, *102*, 062003. [[CrossRef](#)]
149. The LIGO Scientific Collaboration; The Virgo Collaboration A guide to LIGO–Virgo detector noise and extraction of transient gravitational-wave signals. *Class. Quantum Gravity* **2020**, *37*, 055002. [[CrossRef](#)]
150. The LIGO Scientific Collaboration; The Virgo Collaboration Characterization of transient noise in Advanced LIGO relevant to gravitational wave signal GW150914. *Class. Quantum Gravity* **2016**, *33*, 134001. [[CrossRef](#)]

151. The Virgo Collaboration. *Category 1 (CAT1) Data Quality Vetoes Applied to the Analysis of the O3 Run Virgo Data*; Technical Report VIR-0560A-21; 2021. Available online: <https://tds.virgo-gw.eu/ql/?c=16808> (accessed on 11 August 2021).
152. LIGO-Virgo-KAGRA Collaboration Gravitational-Wave Candidate Event Database. Available online: <https://gracedb.ligo.org/> (accessed on 30 June 2021).
153. Turin, G. An introduction to matched filters. *IRE Trans. Inf. Theory* **1960**, *6*, 311–329. [[CrossRef](#)]
154. Messick, C.; Blackburn, K.; Brady, P.; Brockill, P.; Cannon, K.; Cariou, R.; Caudill, S.; Chamberlin, S.J.; Creighton, J.D.E.; Everett, R.; et al. Analysis framework for the prompt discovery of compact binary mergers in gravitational-wave data. *Phys. Rev. D* **2017**, *95*, 042001. [[CrossRef](#)]
155. Nitz, A.; Harry, I.; Brown, D.; Biwer, C.M.; Willis, J.; Dal Canton, T.; Capano, C.; Pekowsky, L.; Dent, T.; Williamson, A.R.; et al. *gwastro/pycbc: PyCBC release v1.16.11*; 2020. [[CrossRef](#)]
156. Aubin, F.; Brighenti, F.; Chierici, R.; Estevez, D.; Greco, G.; Guidi, G.M.; Juste, V.; Marion, F.; Mours, B.; Nitoglia, E.; et al. The MBTA pipeline for detecting compact binary coalescences in the third LIGO–Virgo observing run. *Class. Quantum Gravity* **2021**, *38*, 095004. [[CrossRef](#)]
157. Astone, P.; D’Antonio, S.; Frasca, S.; Palomba, C. A method for detection of known sources of continuous gravitational wave signals in non-stationary data. *Class. Quantum Gravity* **2010**, *27*, 194016. [[CrossRef](#)]
158. Astone, P.; Colla, A.; D’Antonio, S.; Frasca, S.; Palomba, C. Coherent search of continuous gravitational wave signals: Extension of the 5-vectors method to a network of detectors. *J. Phys. Conf. Ser.* **2012**, *363*, 012038. [[CrossRef](#)]
159. Jaranowski, P.; Królak, A.; Schutz, B.F. Data analysis of gravitational-wave signals from spinning neutron stars: The signal and its detection. *Phys. Rev. D* **1998**, *58*. [[CrossRef](#)]
160. Jaranowski, P.; Królak, A. Searching for gravitational waves from known pulsars using the \mathcal{F} and \mathcal{G} statistics. *Class. Quantum Gravity* **2010**, *27*, 194015. [[CrossRef](#)]
161. Dupuis, R.J.; Woan, G. Bayesian estimation of pulsar parameters from gravitational wave data. *Phys. Rev. D* **2005**, *72*, 102002. [[CrossRef](#)]
162. Pitkin, M.; Isi, M.; Veitch, J.; Woan, G. A nested sampling code for targeted searches for continuous gravitational waves from pulsars. *arXiv* **2017**, arXiv:1705.08978.
163. Piccinni, O.J.; Astone, P.; D’Antonio, S.; Frasca, S.; Intini, G.; Leaci, P.; Mastrogiovanni, S.; Miller, A.; Palomba, C.; Singhal, A. A new data analysis framework for the search of continuous gravitational wave signals. *Class. Quantum Gravity* **2018**, *36*, 015008. [[CrossRef](#)]
164. Astone, P.; Colla, A.; D’Antonio, S.; Frasca, S.; Palomba, C. Method for all-sky searches of continuous gravitational wave signals using the frequency-Hough transform. *Phys. Rev. D* **2014**, *90*. [[CrossRef](#)]
165. Krishnan, B.; Sintes, A.M.; Papa, M.A.; Schutz, B.F.; Frasca, S.; Palomba, C. Hough transform search for continuous gravitational waves. *Phys. Rev. D* **2004**, *70*. [[CrossRef](#)]
166. Wette, K.; Walsh, S.; Prix, R.; Papa, M. Implementing a semicoherent search for continuous gravitational waves using optimally constructed template banks. *Phys. Rev. D* **2018**, *97*. [[CrossRef](#)]
167. Brady, P.R.; Creighton, T. Searching for periodic sources with LIGO. II. Hierarchical searches. *Phys. Rev. D* **2000**, *61*, 082001. [[CrossRef](#)]
168. Goetz, E.; Riles, K. An all-sky search algorithm for continuous gravitational waves from spinning neutron stars in binary systems. *Class. Quantum Gravity* **2011**, *28*, 215006. [[CrossRef](#)]
169. Anderson, W.G.; Brady, P.R.; Creighton, J.D.E.; Flanagan, E.E. Excess power statistic for detection of burst sources of gravitational radiation. *Phys. Rev. D* **2001**, *63*, 042003. [[CrossRef](#)]
170. Klimentenko, S.; Yakushin, I.; Mercer, A.; Mitselmakher, G. A coherent method for detection of gravitational wave bursts. *Class. Quantum Gravity* **2008**, *25*, 114029. [[CrossRef](#)]
171. Salemi, F.; Milotti, E.; Prodi, G.A.; Vedovato, G.; Lazzaro, C.; Tiwari, S.; Vinciguerra, S.; Drago, M.; Klimentenko, S. Wider look at the gravitational-wave transients from GWTC-1 using an unmodeled reconstruction method. *Phys. Rev. D* **2019**, *100*, 042003. [[CrossRef](#)]
172. Klimentenko, S.; Vedovato, G.; Drago, M.; Salemi, F.; Tiwari, V.; Prodi, G.A.; Lazzaro, C.; Ackley, K.; Tiwari, S.; Da Silva, C.F.; et al. Method for detection and reconstruction of gravitational wave transients with networks of advanced detectors. *Phys. Rev. D* **2016**, *93*, 042004. [[CrossRef](#)]
173. Lynch, R.; Vitale, S.; Essick, R.; Katsavounidis, E.; Robinet, F. Information-theoretic approach to the gravitational-wave burst detection problem. *Phys. Rev. D* **2017**, *95*, 104046. [[CrossRef](#)]
174. Sutton, P.J.; Jones, G.; Chatterji, S.; Kalmus, P.; Leonor, I.; Poprocki, S.; Rollins, J.; Searle, A.; Stein, L.; Tinto, M.; et al. X-Pipeline: An analysis package for autonomous gravitational-wave burst searches. *New J. Phys.* **2010**, *12*, 053034. [[CrossRef](#)]
175. Suvorova, S.; Sun, L.; Melatos, A.; Moran, W.; Evans, R.J. Hidden Markov model tracking of continuous gravitational waves from a neutron star with wandering spin. *Phys. Rev. D* **2016**, *93*, 123009. [[CrossRef](#)]
176. D’Antonio, S.; Palomba, C.; Frasca, S.; Astone, P.; La Rosa, I.; Leaci, P.; Mastrogiovanni, S.; Piccinni, O.J.; Pierini, L.; Rei, L. Sidereal filtering: A novel robust method to search for continuous gravitational waves. *Phys. Rev. D* **2021**, *103*, 063030. [[CrossRef](#)]
177. Romano, J.D.; Cornish, N.J. Detection methods for stochastic gravitational-wave backgrounds: A unified treatment. *Living Rev. Relativ.* **2017**, *20*. [[CrossRef](#)]

178. Thrane, E.; Kandhasamy, S.; Ott, C.D.; Anderson, W.G.; Christensen, N.L.; Coughlin, M.W.; Dorsher, S.; Giampanis, S.; Mandic, V.; Mytidis, A.; et al. Long gravitational-wave transients and associated detection strategies for a network of terrestrial interferometers. *Phys. Rev. D* **2011**, *83*, 083004. [[CrossRef](#)]
179. Mitra, S.; Dhurandhar, S.; Souradeep, T.; Lazzarini, A.; Mandic, V.; Bose, S.; Ballmer, S. Gravitational wave radiometry: Mapping a stochastic gravitational wave background. *Phys. Rev. D* **2008**, *77*, 042002. [[CrossRef](#)]
180. Zhang, Y.; Papa, M.A.; Krishnan, B.; Watts, A.L. Search for Continuous Gravitational Waves from Scorpius X-1 in LIGO O2 Data. *Astrophys. J.* **2021**, *906*, L14. [[CrossRef](#)]
181. Abbott, B.; Abbott, R.; Abbott, T.; Abraham, S.; Acernese, F.; Ackley, K.; Adams, C.; Adhikari, R.; Adya, V.; Affeldt, C.; et al. Search for gravitational waves from Scorpius X-1 in the second Advanced LIGO observing run with an improved hidden Markov model. *Phys. Rev. D* **2019**, *100*. [[CrossRef](#)]
182. Middleton, H.; Clearwater, P.; Melatos, A.; Dunn, L. Search for gravitational waves from five low mass x-ray binaries in the second Advanced LIGO observing run with an improved hidden Markov model. *Phys. Rev. D* **2020**, *102*. [[CrossRef](#)]
183. Hastings, W.K. Monte Carlo sampling methods using Markov chains and their applications. *Biometrika* **1970**, *57*, 97–109.
184. Metropolis, N.; Rosenbluth, A.W.; Rosenbluth, M.N.; Teller, A.H.; Teller, E. Equation of State Calculations by Fast Computing Machines. *J. Chem. Phys.* **1953**, *21*, 1087–1092.
185. Skilling, J. Nested Sampling. *AIP Conf. Proc.* **2004**, *735*, 395–405.
186. Veitch, J.; Raymond, V.; Farr, B.; Farr, W.; Graff, P.; Vitale, S.; Aylott, B.; Blackburn, K.; Christensen, N.; Coughlin, M.; et al. Parameter estimation for compact binaries with ground-based gravitational-wave observations using the LALInference software library. *Phys. Rev. D* **2015**, *91*, 042003. [[CrossRef](#)]
187. Ashton, G.; Hübner, M.; Lasky, P.D.; Talbot, C.; Ackley, K.; Biscoveanu, S.; Chu, Q.; Divakarla, A.; Easter, P.J.; Goncharov, B.; et al. Bilby: A User-friendly Bayesian Inference Library for Gravitational-wave Astronomy. *Astrophys. J. Suppl. Ser.* **2019**, *241*, 27. [[CrossRef](#)]
188. Biwer, C.M.; Capano, C.D.; De, S.; Cabero, M.; Brown, D.A.; Nitz, A.H.; Raymond, V. PyCBC Inference: A Python-based Parameter Estimation Toolkit for Compact Binary Coalescence Signals. *Publ. Astron. Soc. Pac.* **2019**, *131*, 024503. [[CrossRef](#)]
189. Singer, L.P.; Price, L.R. Rapid Bayesian position reconstruction for gravitational-wave transients. *Phys. Rev. D* **2016**, *93*, 024013. [[CrossRef](#)]
190. Klimentenko, S.; Vedovato, G.; Drago, M.; Mazzolo, G.; Mitselmakher, G.; Pankow, C.; Prodi, G.; Re, V.; Salemi, F.; Yakushin, I. Localization of gravitational wave sources with networks of advanced detectors. *Phys. Rev. D* **2011**, *83*, 102001. [[CrossRef](#)]
191. Cornish, N.J.; Littenberg, T.B. Bayeswave: Bayesian inference for gravitational wave bursts and instrument glitches. *Class. Quantum Gravity* **2015**, *32*, 135012.
192. Littenberg, T.B.; Cornish, N.J. Bayesian inference for spectral estimation of gravitational wave detector noise. *Phys. Rev. D* **2015**, *91*, 084034. [[CrossRef](#)]
193. The LIGO Scientific Collaboration; The Virgo Collaboration All-Sky Search for Short Gravitational-Wave Bursts in the Second Advanced LIGO and Advanced Virgo Run. *Phys. Rev. D* **2019**, *100*, 024017.
194. The LIGO Scientific Collaboration; The Virgo Collaboration All-sky search for short gravitational-wave bursts in the first Advanced LIGO run. *Phys. Rev. D* **2017**, *95*, 042003.
195. The LIGO Scientific Collaboration; The Virgo Collaboration All-sky search for long-duration gravitational wave transients in the first Advanced LIGO observing run. *Class. Quantum Gravity* **2018**, *35*, 065009. [[CrossRef](#)]
196. The LIGO Scientific Collaboration; The Virgo Collaboration All-sky search for long-duration gravitational-wave transients in the second Advanced LIGO observing run. *Phys. Rev. D* **2019**, *99*, 104033. [[CrossRef](#)]
197. The LIGO Scientific Collaboration; The Virgo Collaboration Low-latency Gravitational-wave Alerts for Multimessenger Astronomy during the Second Advanced LIGO and Virgo Observing Run. *Astrophys. J.* **2019**, *875*, 161.
198. Kelley, L.Z.; Mandel, I.; Ramirez-Ruiz, E. Electromagnetic transients as triggers in searches for gravitational waves from compact binary mergers. *Phys. Rev. D* **2013**, *87*, 123004.
199. Harry, I.W.; Fairhurst, S. Targeted coherent search for gravitational waves from compact binary coalescences. *Phys. Rev. D* **2011**, *83*, 084002. [[CrossRef](#)]
200. Williamson, A.R.; Biwer, C.; Fairhurst, S.; Harry, I.W.; Macdonald, E.; Macleod, D.; Predoi, V. Improved methods for detecting gravitational waves associated with short gamma-ray bursts. *Phys. Rev. D* **2014**, *90*, 122004. [[CrossRef](#)]
201. LIGO Scientific Collaboration. *LIGO Algorithm Library—LALSuite*; Free Software (GPL); LIGO Scientific Collaboration: Pasadena, CA, USA, 2018. [[CrossRef](#)]
202. Was, M.; Sutton, P.J.; Jones, G.; Leonor, I. Performance of an externally triggered gravitational-wave burst search. *Phys. Rev. D* **2012**, *86*, 022003.
203. Urban, A. *Monsters in the Dark: High Energy Signatures of Black Hole Formation with Multimessenger Astronomy*. Ph.D. Thesis, University of Wisconsin-Milwaukee, 2016.
204. Gehrels, N.; Chincarini, G.; Giommi, P.; Mason, K.O.; Nousek, J.A.; Wells, A.A.; White, N.E.; Barthelmy, S.D.; Burrows, D.N.; Cominsky, L.R.; et al. The Swift Gamma-Ray Burst Mission. *Astrophys. J.* **2004**, *611*, 1005–1020.
205. Countryman, S.; Keivani, A.; Bartos, I.; Marka, Z.; Kintscher, T.; Corley, R.; Blaufuss, E.; Finley, C.; Marka, S. Low-Latency Algorithm for Multi-messenger Astrophysics (LLAMA) with Gravitational-Wave and High-Energy Neutrino Candidates. *arXiv* **2019**, arXiv:1901.05486.

206. Abdollahi, S.; Acero, F.; Ackermann, M.; Ajello, M.; Atwood, W.B.; Axelsson, M.; Baldini, L.; Ballet, J.; Barbiellini, G.; Bastieri, D.; et al. Fermi Large Area Telescope Fourth Source Catalog. *Astrophys. J. Suppl. Ser.* **2020**, *247*, 33. [[CrossRef](#)]
207. The LIGO Scientific Collaboration; The Virgo Collaboration; The KAGRA Collaboration Search for anisotropic gravitational-wave backgrounds using data from Advanced LIGO's and Advanced Virgo's first three observing runs. *Phys. Rev. D* **2021**, *104*, 022005. [[CrossRef](#)]
208. Fermi-LAT Collaboration Characterizing the population of pulsars in the inner Galaxy with the Fermi Large Area Telescope. *arXiv* **2017**, arXiv:1705.00009.
209. Abramowski, A.; Aharonian, F.; Benkhali, F. Ait; Akhperjanian, A. G.; Angüner, E. O.; Backes, M.; Balzer, A.; Becherini, Y.; Tjus, J.B.; Berge, D.; et al. Acceleration of peta-electronvolt protons in the Galactic Centre. *Nature* **2016**, *531*, 476–479. [[CrossRef](#)]
210. H.E.S.S. collaboration The Fermi Galactic Center GeV Excess and Implications for Dark Matter. *Astrophys. J.* **2017**, *840*, 43. [[CrossRef](#)]
211. The LIGO Scientific Collaboration; The Virgo Collaboration GW190425: Observation of a Compact Binary Coalescence with Total Mass $\sim 3.4 M_{\odot}$. *Astrophys. J. Lett.* **2020**, *892*, L3.
212. The LIGO Scientific Collaboration; The Virgo Collaboration GW190412: Observation of a binary-black-hole coalescence with asymmetric masses. *Phys. Rev. D* **2020**, *102*, 043015. [[CrossRef](#)]
213. The LIGO Scientific Collaboration; The Virgo Collaboration GW190814: Gravitational Waves from the Coalescence of a 23 Solar Mass Black Hole with a 2.6 Solar Mass Compact Object. *Astrophys. J. Lett.* **2020**, *896*, L44.
214. The LIGO Scientific Collaboration; The Virgo Collaboration GW190521: A Binary Black Hole Merger with a Total Mass of $150 M_{\odot}$. *Phys. Rev. D* **2020**, *125*, 101102.
215. The LIGO Scientific Collaboration; The Virgo Collaboration Search for lensing signatures in the gravitational-wave observations from the first half of LIGO-Virgo's third observing run. *arXiv* **2021**, arXiv:2105.06384.
216. The LIGO Scientific Collaboration; The Virgo Collaboration Population Properties of Compact Objects from the Second LIGO-Virgo Gravitational-Wave Transient Catalog. *Astrophys. J. Lett.* **2021**, *913*, L7.
217. The LIGO Scientific Collaboration; The Virgo Collaboration Observation of Gravitational Waves from Two Neutron Star-Black Hole Coalescences. *Astrophys. J. Lett.* **2021**, *915*, L5. [[CrossRef](#)]
218. Hosseinzadeh, G.; Cowperthwaite, P.S.; Gomez, S.; Villar, V.A.; Nicholl, M.; Margutti, R.; Berger, E.; Chornock, R.; Paterson, K.; Fong, W.; et al. Follow-up of the Neutron Star Bearing Gravitational-wave Candidate Events S190425z and S190426c with MMT and SOAR. *Astrophys. J. Lett.* **2019**, *880*, L4.
219. Andreoni, I.; Goldstein, D.A.; Kasliwal, M.M.; Nugent, P.E.; Zhou, R.; Newman, J.A.; Bulla, M.; Foucart, F.; Hotokezaka, K.; Nakar, E.; et al. GROWTH on S190814bv: Deep Synoptic Limits on the Optical/Near-infrared Counterpart to a Neutron Star-Black Hole Merger. *Astrophys. J.* **2020**, *890*, 131.
220. Goldstein, A.; Veres, P.; Burns, E.; Briggs, M.S.; Hamburg, R.; Kocevski, D.; Wilson-Hodge, C.A.; Preece, R.D.; Poolakkil, S.; Roberts, O.J.; et al. An Ordinary Short Gamma-Ray Burst with Extraordinary Implications: Fermi-GBM Detection of GRB 170817A. *Astrophys. J. Lett.* **2017**, *848*, L14.
221. Savchenko, V.; Ferrigno, C.; Kuulkers, E.; Bazzano, A.; Bozzo, E.; Brandt, S.; Chenevez, J.; Courvoisier, T.J.L.; Diehl, R.; Domingo, A.; et al. INTEGRAL Detection of the First Prompt Gamma-Ray Signal Coincident with the Gravitational-wave Event GW170817. *Astrophys. J. Lett.* **2017**, *848*, L15.
222. LIGO Scientific Collaboration; Virgo Collaboration; Fermi Gamma-Ray Burst Monitor; INTEGRAL Gravitational Waves and Gamma-Rays from a Binary Neutron Star Merger: GW170817 and GRB 170817A. *Astrophys. J. Lett.* **2017**, *848*, L13.
223. Abbott, B.P.; Abbott, R.; Abbott, T.D.; Acernese, F.; Ackley, K.; Adams, C.; Adams, T.; Addesso, P.; Adhikari, R.X.; Adya, V. B.; et al. Multi-messenger Observations of a Binary Neutron Star Merger. *Astrophys. J. Lett.* **2017**, *848*, L12.
224. Coulter, D.A.; Kilpatrick, C.D.; Siebert, M.R.; Foley, R.J.; Shappee, B.J.; Drout, M.R.; Simon, J.S.; Piro, A.L.; Rest, A. One-Meter Two-Hemisphere (1M2H) Collaboration. LIGO/Virgo G298048: Potential optical counterpart discovered by Swope telescope. *GRB Coord. Netw.* **2017**, *21529*, 1.
225. Pian, E.; D'Avanzo, P.; Benetti, S.; Branchesi, M.; Brocato, E.; Campana, S.; Cappellaro, E.; Covino, S.; D'Elia, V.; Fynbo, J.P.U.; et al. Spectroscopic identification of r-process nucleosynthesis in a double neutron-star merger. *Nature* **2017**, *551*, 67–70.
226. Smartt, S.J.; Chen, T.W.; Jerkstrand, A.; Coughlin, M.; Kankare, E.; Sim, S.A.; Fraser, M.; Inerra, C.; Maguire, K.; Chambers, K.C.; et al. A kilonova as the electromagnetic counterpart to a gravitational-wave source. *Nature* **2017**, *551*, 75–79.
227. Troja, E.; Piro, L.; van Eerten, H.; Wollaeger, R.T.; Im, M.; Fox, O.D.; Butler, N.R.; Cenko, S.B.; Sakamoto, T.; Fryer, C.L.; et al. The X-ray counterpart to the gravitational-wave event GW170817. *Nature* **2017**, *551*, 71–74.
228. Hallinan, G.; Corsi, A.; Mooley, K.P.; Hotokezaka, K.; Nakar, E.; Kasliwal, M.M.; Kaplan, D.L.; Frail, D.A.; Myers, S.T.; Murphy, T.; et al. A radio counterpart to a neutron star merger. *Science* **2017**, *358*, 1579–1583.
229. Mooley, K.P.; Deller, A.T.; Gottlieb, O.; Nakar, E.; Hallinan, G.; Bourke, S.; Frail, D.A.; Horesh, A.; Corsi, A.; Hotokezaka, K. Superluminal motion of a relativistic jet in the neutron-star merger GW170817. *Nature* **2018**, *561*, 355–359.
230. Ghirlanda, G.; Salafia, O.S.; Paragi, Z.; Giroletti, M.; Yang, J.; Marcote, B.; Blanchard, J.; Agudo, I.; An, T.; Bernardini, M.G.; et al. Compact radio emission indicates a structured jet was produced by a binary neutron star merger. *Science* **2019**, *363*, 968–971.
231. Abbott, B.P.; Abbott, R.; Abbott, T.D.; Acernese, F.; Ackley, K.; Adams, C.; Adams, T.; Addesso, P.; Adhikari, R.X.; Adya, V.B.; et al. A gravitational-wave standard siren measurement of the Hubble constant. *Nature* **2017**, *551*, 85–88.

232. Freedman, W.L.; Madore, B.F.; Gibson, B.K.; Ferrarese, L.; Kelson, D.D.; Sakai, S.; Mould, J.R.; Kennicutt, Robert C.J.; Ford, H.C.; Graham, J.A.; et al. Final Results from the Hubble Space Telescope Key Project to Measure the Hubble Constant. *Astrophys. J.* **2001**, *553*, 47–72.
233. Riess, A.G.; Macri, L.M.; Hoffmann, S.L.; Scolnic, D.; Casertano, S.; Filippenko, A.V.; Tucker, B.E.; Reid, M.J.; Jones, D.O.; Silverman, J.M.; et al. A 2.4% Determination of the Local Value of the Hubble Constant. *Astrophys. J.* **2016**, *826*, 56.
234. Planck Collaboration Planck 2015 results. XIII. Cosmological parameters. *Astron. Astrophys.* **2016**, *594*, A13.
235. Abbott, B.P.; Abbott, R.; Abbott, T.D.; Acernese, F.; Ackley, K.; Adams, C.; Adams, T.; Addesso, P.; Adhikari, R.X.; Adya, V.B.; et al. GW170817: Measurements of Neutron Star Radii and Equation of State. *Phys. Rev. Lett.* **2018**, *121*. [[CrossRef](#)]
236. Abbott, R.; Abbott, T.; Abraham, S.; Acernese, F.; Ackley, K.; Adams, A.; Adams, C.; Adhikari, R.; Adya, V.; Affeldt, C.; et al. Tests of general relativity with binary black holes from the second LIGO-Virgo gravitational-wave transient catalog. *Phys. Rev. D* **2021**, *103*. [[CrossRef](#)]
237. Yunes, N.; Yagi, K.; Pretorius, F. Theoretical physics implications of the binary black-hole mergers GW150914 and GW151226. *Phys. Rev. D* **2016**, *94*, 084002. [[CrossRef](#)]
238. Nair, R.; Perkins, S.; Silva, H.O.; Yunes, N. Fundamental Physics Implications for Higher-Curvature Theories from Binary Black Hole Signals in the LIGO-Virgo Catalog GWTC-1. *Phys. Rev. Lett.* **2019**, *123*, 191101. [[CrossRef](#)] [[PubMed](#)]
239. Abbott, B.; Abbott, R.; Abbott, T.; Abraham, S.; Acernese, F.; Ackley, K.; Adams, C.; Adhikari, R.; Adya, V.; Affeldt, C.; et al. Tests of general relativity with the binary black hole signals from the LIGO-Virgo catalog GWTC-1. *Phys. Rev. D* **2019**, *100*. [[CrossRef](#)]
240. Ho, W.C.G.; Espinoza, C.M.; Arzoumanian, Z.; Enoto, T.; Tamba, T.; Antonopoulou, D.; Bejger, M.; Guillot, S.; Haskell, B.; Ray, P.S. Return of the Big Glitcher: NICER timing and glitches of PSR J0537-6910. *Mon. Not. R. Astron. Soc.* **2020**, *498*, 4605–4614. [[CrossRef](#)]
241. The LIGO Scientific Collaboration; The Virgo Collaboration; The KAGRA Collaboration; All-sky Search for Continuous Gravitational Waves from Isolated Neutron Stars in the Early O3 LIGO Data. *Phys. Rev. D* **2021**, *103*, 064017. [[CrossRef](#)]
242. Dergachev, V.; Papa, M.A. Results from the First All-Sky Search for Continuous Gravitational Waves from Small-Ellipticity Sources. *Phys. Rev. Lett.* **2020**, *125*, 171101. [[CrossRef](#)] [[PubMed](#)]
243. Dergachev, V.; Papa, M.A. The search for continuous gravitational waves from small-ellipticity sources at low frequencies. *arXiv* **2021**, arXiv:2104.09007.
244. Steltner, B.; Papa, M.A.; Eggenstein, H.B.; Allen, B.; Dergachev, V.; Prix, R.; Machenschalk, B.; Walsh, S.; Zhu, S.J.; Behnke, O.; et al. Einstein@Home All-sky Search for Continuous Gravitational Waves in LIGO O2 Public Data. *Astrophys. J.* **2021**, *909*, 79. [[CrossRef](#)]
245. Dergachev, V.; Papa, M.A. Results from high-frequency all-sky search for continuous gravitational waves from small-ellipticity sources. *Phys. Rev. D* **2021**, *103*. [[CrossRef](#)]
246. The LIGO Scientific Collaboration; The Virgo Collaboration; The KAGRA Collaboration; Upper Limits on the Isotropic Gravitational-Wave Background from Advanced LIGO's and Advanced Virgo's Third Observing Run. *Phys. Rev. D* **2021**, *104*, 022004. [[CrossRef](#)]
247. Palomba, C.; D'Antonio, S.; Astone, P.; Frasca, S.; Intini, G.; La Rosa, I.; Leaci, P.; Mastrogiovanni, S.; Miller, A.L.; Muciaccia, F.; et al. Direct Constraints on the Ultralight Boson Mass from Searches of Continuous Gravitational Waves. *Phys. Rev. Lett.* **2019**, *123*, 171101. [[CrossRef](#)] [[PubMed](#)]
248. Ng, K.K.Y.; Vitale, S.; Hannuksela, O.A.; Li, T.G.F. Constraints on Ultralight Scalar Bosons within Black Hole Spin Measurements from the LIGO-Virgo GWTC-2. *Phys. Rev. Lett.* **2021**, *126*. [[CrossRef](#)]
249. Bustillo, J.C.; Sanchis-Gual, N.; Torres-Forné, A.; Font, J.A.; Vajpeyi, A.; Smith, R.; Herdeiro, C.; Radu, E.; Leong, S.H.W. GW190521 as a Merger of Proca Stars: A Potential New Vector Boson of 8.7×10^{-13} eV. *Phys. Rev. Lett.* **2021**, *126*, 081101. [[CrossRef](#)]
250. The LIGO Scientific Collaboration; The Virgo Collaboration; The KAGRA Collaboration. Constraints on dark photon dark matter using data from LIGO's and Virgo's third observing run. *arXiv* **2021**, arXiv:2105.13085.
251. Guo, H.K.; Riles, K.; Yang, F.W.; Zhao, Y. Searching for dark photon dark matter in LIGO O1 data. *Commun. Phys.* **2019**, *2*. [[CrossRef](#)]
252. Kibble, T.W.B. Topology of cosmic domains and strings. *J. Phys. A Math. Gen.* **1976**, *9*, 1387–1398. [[CrossRef](#)]
253. Jeannerot, R.; Rocher, J.; Sakellariadou, M. How generic is cosmic string formation in supersymmetric grand unified theories. *Phys. Rev. D* **2003**, *68*, 103514. [[CrossRef](#)]
254. Sakellariadou, M. Gravitational waves emitted from infinite strings. *Phys. Rev. D* **1990**, *42*, 354–360. [[CrossRef](#)] [[PubMed](#)]
255. Vachaspati, T.; Vilenkin, A. Gravitational radiation from cosmic strings. *Phys. Rev. D* **1985**, *31*, 3052–3058. [[CrossRef](#)]
256. Vilenkin, A. Gravitational radiation from cosmic strings. *Phys. Lett. B* **1981**, *107*, 47–50. [[CrossRef](#)]
257. Abbott, R.; Abbott, T.D.; Abraham, S.; Acernese, F.; Ackley, K.; Adams, A.; Adams, C.; Adhikari, R.X.; Adya, V.B.; Affeldt, C.; et al. Constraints on Cosmic Strings Using Data from the Third Advanced LIGO–Virgo Observing Run. *Phys. Rev. Lett.* **2021**, *126*, 241102. [[CrossRef](#)] [[PubMed](#)]
258. The LIGO Scientific Collaboration; The Virgo Collaboration Constraints on cosmic strings using data from the first Advanced LIGO observing run. *Phys. Rev. D* **2018**, *97*, 102002. [[CrossRef](#)]
259. Abbott, B.P.; Abbott, R.; Abbott, T.D.; Abraham, S.; Acernese, F. Search for the isotropic stochastic background using data from Advanced LIGO's second observing run. *Phys. Rev. D* **2019**, *100*, 061101. [[CrossRef](#)]
260. Abbott, B.P.; Abbott, R.; Abbott, T.D.; Abernathy, M.R. Upper Limits on the Stochastic Gravitational-Wave Background from Advanced LIGO's First Observing Run. *Phys. Rev. Lett.* **2017**, *118*, 121101. [[CrossRef](#)] [[PubMed](#)]

261. The Virgo Collaboration. *Advanced Virgo Plus Phase I—Design Report*; Technical Report VIR-0596A-19; 2019. Available online: <https://tds.virgo-gw.eu/ql/?c=14430> (accessed on 11 August 2021).
262. Chelkowski, S.; Vahlbruch, H.; Hage, B.; Franzen, A.; Lastzka, N.; Danzmann, K.; Schnabel, R. Experimental characterization of frequency-dependent squeezed light. *Phys. Rev. A* **2005**, *71*, 013806. [[CrossRef](#)]
263. Oelker, E.; Isogai, T.; Miller, J.; Tse, M.; Barsotti, L.; Mavalvala, N.; Evans, M. Audio-band frequency-dependent squeezing for gravitational-wave detectors. *Phys. Rev. Lett.* **2016**, *116*, 041102. [[CrossRef](#)]
264. Zhao, Y.; Aritomi, N.; Capocasa, E.; Leonardi, M.; Eisenmann, M.; Guo, Y.; Polini, E.; Tomura, A.; Arai, K.; Aso, Y.; et al. Frequency-Dependent Squeezed Vacuum Source for Broadband Quantum Noise Reduction in Advanced Gravitational-Wave Detectors. *Phys. Rev. Lett.* **2020**, *124*, 171101. [[CrossRef](#)] [[PubMed](#)]
265. Capocasa, E.; Barsuglia, M.; Degallaix, J.; Pinard, L.; Straniero, N.; Schnabel, R.; Somiya, K.; Aso, Y.; Tatsumi, D.; Flaminio, R. Estimation of losses in a 300 m filter cavity and quantum noise reduction in the KAGRA gravitational-wave detector. *Phys. Rev. D* **2016**, *93*, 082004. [[CrossRef](#)]
266. McCuller, L.; Whittle, C.; Ganapathy, D.; Komori, K.; Tse, M.; Fernandez-Galiana, A.; Barsotti, L.; Fritschel, P.; MacInnis, M.; Matichard, F.; et al. Frequency-dependent squeezing for advanced LIGO. *Phys. Rev. Lett.* **2020**, *124*, 171102. [[CrossRef](#)] [[PubMed](#)]
267. Sequino, V. Quantum noise reduction in Advanced Virgo. *Phys. Scr.* **2021**, *96*, 104014. [[CrossRef](#)]
268. Mullavey, A.J.; Slagmolen, B.J.J.; Miller, J.; Evans, M.; Fritschel, P.; Sigg, D.; Waldman, S.J.; Shaddock, D.A.; McClelland, D.E. Arm-length stabilisation for interferometric gravitational-wave detectors using frequency-doubled auxiliary lasers. *Opt. Express* **2012**, *20*, 81–89. [[CrossRef](#)]
269. Izumi, K.; Arai, K.; Barr, B.; Betzwieser, J.; Brooks, A.; Dahl, K.; Doravari, S.; Driggers, J.C.; Korth, W.Z.; Miao, H.; et al. Multicolor cavity metrology. *J. Opt. Soc. Am. A* **2012**, *29*, 2092–2103. [[CrossRef](#)]
270. Staley, A.; Martynov, D.; Abbott, R.; Adhikari, R.X.; Arai, K.; Ballmer, S.; Barsotti, L.; Brooks, A.F.; DeRosa, R.T.; Dwyer, S.; et al. Achieving resonance in the Advanced LIGO gravitational-wave interferometer. *Class. Quantum Gravity* **2014**, *31*, 245010. [[CrossRef](#)]
271. Akutsu, T.; Ando, M.; Arai, K.; Arai, K.; Arai, Y.; Araki, S.; Araya, A.; Aritomi, N.; Aso, Y.; Bae, S.; et al. An arm length stabilization system for KAGRA and future gravitational-wave detectors. *Class. Quantum Gravity* **2020**, *37*, 035004. [[CrossRef](#)]
272. De Rossi, C.; Brooks, J.; Casanueva Diaz, J.; Chiummo, A.; Genin, E.; Gosselin, M.; Leroy, N.; Mantovani, M.; Montanari, B.; Nocera, F.; et al. Development of a Frequency Tunable Green Laser Source for Advanced Virgo+ Gravitational Waves Detector. *Galaxies* **2020**, *8*, 87. [[CrossRef](#)]
273. Cesarini, E.; Lorenzini, M.; Amato, A.; Cagnoli, G.; Cassar, Q.; Dickmann, J.; Granata, M.; Fafone, V.; Heinert, D.; Kroker, S.; et al. The Virgo Coating Collaboration: A detailed study on thermoelasticity in crystalline materials and other research lines. PoS, Proceedings of the GRAvitational-wave Science&technology Symposium 2018 (GRASS2018), Padova, Italy, 1–2 March 2018. [[CrossRef](#)]
274. Harry, G.M.; Gretarsson, A.M.; Saulson, P.R.; Kittelberger, S.E.; Penn, S.D.; Startin, W.J.; Rowan, S.; Fejer, M.M.; Crooks, D.R.M.; Cagnoli, G.; et al. Thermal noise in interferometric gravitational wave detectors due to dielectric optical coatings. *Class. Quantum Gravity* **2002**, *19*, 897–917. [[CrossRef](#)]
275. Granata, M.; Coillet, E.; Martinez, V.; Dolique, V.; Amato, A.; Canepa, M.; Margueritat, J.; Martinet, C.; Mermet, A.; Michel, C.; et al. Correlated evolution of structure and mechanical loss of a sputtered silica film. *Phys. Rev. Mater.* **2018**, *2*, 053607. [[CrossRef](#)]
276. Puosi, F.; Fidecaro, F.; Capaccioli, S.; Pisignano, D.; Leporini, D. In silico broadband mechanical spectroscopy of amorphous tantalum. *Phys. Rev. Res.* **2019**, *1*, 033121. [[CrossRef](#)]
277. Amato, A.; Terreni, S.; Granata, M.; Michel, C.; Sassolas, B.; Pinard, L.; Canepa, M.; Cagnoli, G. Observation of a Correlation Between Internal friction and Urbach Energy in Amorphous Oxides Thin Films. *Sci. Rep.* **2020**, *10*, 1670. [[CrossRef](#)] [[PubMed](#)]